Investigation of Double-Pulsed Gas Metal Arc Welding Technique to Preclude Carbide Precipitates in Aerospace Grade Hastelloy X

M. Sathishkumar, Yash Jitendra Bhakat, K. Gokul Kumar, S. Giribaskar, R. Oyyaravelu, N. Arivazhagan, and M. Manikandan ⬤

Hastelloy X develops hot fissuring during fusion welding, which could be precluded using single-pulsed gas metal arc welding (SP-GMAW) and double-pulsed gas metal arc welding (DP-GMAW). The outcome of this research is to provide a better insight into microstructural characteristics, and mechanical properties of Hastelloy X welded by GMAW, SP-GMAW, and DP-GMAW techniques. GMAW depicts the cellular dendrites, whereas DP-GMAW and SP-GMAW displayed fine equiaxed dendrites. Mo-rich segregation is identified in the interdendritic region of GMAW owing to high solidification time. Mo-rich segregation is reduced for SP-GMAW, whereas it is completely precluded for DP-GMAW due to the existence of refined grain. The development of M_3C (Fe_2MoC) and M_6C (Fe_2Mo_4C) carbide precipitates is identified in GMAW and SP-GMAW. But, DP-GMAW displays the absence of Mo-rich carbides and the development of Mo_1Ni_4 intermetallic precipitates. DP-GMAW provides better joint efficiency (96.32%), UTS, and ductility, which is followed by SP-GMAW and GMAW. DP-GMAW shows higher mean microhardness (7.31% and 3.52%) and impact toughness (49.01% and 26.67%) on comparison with GMAW and SP-GMAW, respectively. Inverse pole figure (IPF) maps of SP-GMAW weldment confirmed that the broad and straight dendrites formed tend to grow along $< 100 >$ direction during the entire solidification process. DP-GMAW also displays the major intensity shift from $< 100 >$ to $< 111 >$ direction. Evidence for the formation of equiaxed grains of random orientation along with dendrites is confirmed by IPF maps from DP-GMAW weldments. The presence of these equiaxed grains in the DP-GMAW weldment might have contributed to the enhancement of tensile properties.

1. Introduction

In modern days, the aerospace components are operated at very high temperatures, and the operating materials have to sustain very high strength, oxidation, and corrosion resistance. The selection of Ni-based alloys is highly suitable for this environment. Especially, Hastelloy X (Ni-Cr-Fe-Mo) is majorly used in the above application, and it is strengthened by a solid solution strengthening technique. It is majorly utilised in gas turbine parts, aerospace components (afterburner, tailpipe, combustion chamber, thrust reverser), and high-temperature gas-cooled reactor (Ref. 1-4). The existence of Fe, Cr, and Mo is providing exceptional corrosion resistance, strength, and oxidation resistance even up to 1200 °C (Ref. 5).

The Hastelloy X can be repaired or fabricated with the fusion welding technique. The long workpieces can be effectively welded with better penetration, higher deposition rate by the gas metal arc welding (GMAW) process when compared to other types of fusion welding techniques (Ref. 6, 7). However, during solidification, Hastelloy X creates secondary carbide precipitates such as $M_{23}C_6$, σ, M_6C, and μ. These precipitates are rich in Mo and Cr contents and act as the nucleation spots for the hot cracking initiation (Ref. 8-10). Ojo et al. (Ref. 11) reported micro-fissuring of Ni-base alloy (Inconel 738) and the presence of the $M_{23}X_6$ carbide phase. Also, the authors observed the grain coarsening effect of gamma prime phases. These carbides create the low melting constituents in the interdendritic region, which further promotes the hot cracks during solidification. Baek et al. (Ref. 12) studied thermochemical deterioration of Hastelloy X. The authors reported the continuous film of topologically close-packed (TCP) phases in the interdendritic region. These carbide phases act as hot fissuring in the weldment which deteriorates the mechanical behaviour of Hastelloy X. Sihotang et al. (Ref. 13) investigated the influence of heat supply on microstructural changes occurred during gas tungsten arc welding (GTAW). The authors concluded that, in low heat supply, the carbide precipitates such as σ, *P* were dissolved into the matrix. Whereas at higher heat supply, σ and *P* phases create coarser intergranular film at the interdendritic region. These carbide phases forming along the grain boundaries deteriorate the tensile strength.

M. Sathishkumar, Department of Mechanical Engineering, Amrita School of Engineering, Amrita Vishwa Vidyapeetham, Chennai, India; and School of Mechanical Engineering, Vellore Institute of Technology, Vellore, India; **Yash Jitendra Bhakat, K. Gokul Kumar, R. Oyyaravelu, N. Arivazhagan,** and **M. Manikandan**, School of Mechanical Engineering, Vellore Institute of Technology, Vellore, India; **S. Giribaskar**, Advanced Forming Research Centre, National Manufacturing Institute Scotland, University of Strathclyde, Glasgow PA4 9LJ, UK. Contact e-mail: mano.manikandan@gmail.com.

Mohammad Reza Abedi et al. (Ref. 14) reported the effect of repair welding of Hastelloy X by GTAW. The authors concluded the presence of $M_{23}C_6$ and M_6C carbide precipitates. Zhao et al. (Ref. 15) developed the phase precipitation and time-temperature diagram for Hastelloy X. Authors concluded the existence of the P, σ, $M_{23}C_6$, and M_6C carbide precipitates. Shigeki Shimizu et al. (Ref. 16) investigated the weldability of Hastelloy X by electron beam welding. They concluded that the micro-cracks and porosities developing in the weldments could be overcome by supplying the proper heat input. Dacian Tomus et al. (Ref. 17) reported that the cracks were initiated and propagated due to the hot tearing and accumulation of internal strain.

From the literature mentioned above, it is realised that there is a huge need to develop the welding technique, which impedes the development of Mo-rich and Cr-rich secondary carbide precipitates such as $M_{23}C_6$, σ, M_6C, and μ. Development of these precipitates during welding creates the liquation and solidification (hot crack) cracking in the weldment. Due to the development of these intermetallic precipitates, the strength and ductility of the weldment are drastically reduced. In the way to resolve these issues, the selection of optimum welding process parameters and suitable welding technique must be done to achieve defect-free weldments. In the present research, welding of Hastelloy X, by adopting three different welding, namely GMAW, SP-GMAW, and DP-GMAW, using ERNiCr-Mo-2 filler, is investigated. In order to sort out the problem of dilution during welding, the base metal filler wire has opted for this study. Single pulse and double pulse welding techniques were adopted to understand their influence on microstructure and mechanical properties of weldments.

The following literature alleviates the formation of intermetallic precipitates using single pulse and double pulse arc welding techniques.

In recent manufacturing techniques, arc welding is playing a significant role in the welding of ferrous and non-ferrous materials. Especially in welding of high strength material such as Ni-base alloys, the selection of welding technique and optimum welding parameters need to be identified to achieve defect-free welding. GMAW technique provides a higher deposition rate, full penetration, but still, this will not enhance the strength of weldment due to higher heat input. Whereas a different version of GMAW like the SP-GMAW technique is giving better results due to the supply of pulsed current instead of continuous current. This pulsed current reduces the amount of heat supplied by reducing the mean current, and this gives benefits such as lower spatter, deeper penetration, higher deposition rates, and larger welding speed. More importantly, SP-GMAW reduces porosity and other defects (Ref. 18). Even better results are observed with the use of the DP-GMAW technique as compared to SP-GMAW. In this method, each cycle of the thermal strong and thermal weak pulse consists of many numbers of peaks and background pulses inside. This further reduces the mean current supply compared to SP-GMAW. The DP-GMAW technique has the following advantages when compared to GMAW and SP-GMAW: (i) minimise crack sensitivity, (ii) ability to perform all position welding, (iii) minimise the total heat input provided, (iv) enhances the joint properties, and (v) wider adjusting range and root gap design (Ref. 19). The better outcomes observed from DP-GMAW are to be used for joining the combustion chamber parts of JT9D turbojet engine, placed in the Boeing aircraft.

Sathishkumar et al. (Ref. 20, 21) reported the advantages of pulsed current gas tungsten arc welding (PC-GTAW) of Hastelloy X using ERNiCrCoMo-1 and ERNiCrMo-2 to preclude carbides in the weldment. It was confirmed that the segregations of carbide phases were suppressed during pulse current mode, which reduces the liquation and solidification cracks. Mainak sen et al. (Ref. 19) reported that the effects of microstructure and hardness variation during double pulse welding of the low carbon steel with different combinations of welding parameters. The authors concluded that in low heat input conditions, finer grains were observed in the weld centre (WC) as well as in the heat-affected zone (HAZ). The finer grains in the HAZ and weld centre led to higher hardness values for weldment as compared to the base metal. Wang et al. (Ref. 22) studied the DP-GMAW technique and concluded that the increased cooling rates due to low heat input improved the degree of grain refinement. Similar observations were reported by Wang et al. (Ref. 23) and claimed that the higher solidification rate and cooling rate observed during the DP-GMAW technique led to grain refinement in the weldment.

Anhua Liu et al. (Ref. 24) investigated the properties of AA5754 Al-alloy by the DP-GMAW technique. The greater number of droplet transfer in thermal pulse than the thermal base enhances the grain size refinement, and it improves the mechanical properties. Mathivanan et al. (Ref. 25) studied the effects of single and double pulse welding on 310SS austenitic stainless steel. The outcomes confirmed that the DP-GMAW technique enhances weld bead quality and associated mechanical properties. This is due to low heat input and reduced thermal shrinkage as compared to the SP-GMAW technique. Palani et al. (Ref. 26) reported the selection of welding parameters such as peak current, base current, peak duration, base time, and frequency of SP-GMAW technique to obtain better results. Kaiyun Wu et al. (Ref. 27) studied SP-GMAW and DP-GMAW technique on mechanical properties of the weldment. Authors concluded that more stable and better weld bead quality, refined grains, and higher hardness were observed for DP-GMAW than SP-GMAW.

From the above literature, the double pulsing welding method is expected to preclude the segregation of Cr-rich and Mo-rich carbide precipitates that further avoided the development of hot cracks in the weldment. Hitherto, not much research work has been carried out related to the welding of Hastelloy X with double pulse condition, which precludes the development of secondary carbide phases like $M_{23}C_6$, M_6C, σ, P during solidification as well as prevents the weldment from hot fissuring. The objective of current work is to preclude the Mo-rich and Cr-rich precipitates in the Hastelloy X weld joints by DP-GMAW method. Then, its effects on the metallurgical and mechanical properties are to be compared with GMAW and SP-GMAW techniques.

2. Welding Materials and Methods

2.1 Hastelloy X and GMAW

The Hastelloy X plate with a shape of 500 mm × 150 mm x 7 mm was procured in a solution heat-treated state. The impurities, such as oil and dirt on the received plate, were cleaned by applying acetone over the plate. The elemental weight percentage of the received material was tested by optical

emission spectroscopy (OES), using the sample of 10 mm x 10 mm x 7 mm size through the wire cut electric discharge machine (W-EDM). The results of the chemical composition of Hastelloy X are displayed in Table 1. For welding, the plate with a dimension of 150 mm x 55 mm x 7 mm was sliced from the received plate by W-EDM. The milling machine was used to prepare the single V-groove on the plate with a 30° of bevel angle and 2 mm of root gap. After that, the samples were put inside the mixture of HCl and water solution to vanish the foreign particles. The samples were rigidly fixed over the copper plates with the use of a C-clamp to control the distortion. The welding of samples has been done in three different conditions, such as conventional GMAW (gas metal arc welding), SP-GMAW (single pulse), and DP-GMAW (double pulse) using ERNiCrMo-2. The electron gun spectroscopy was used to determine the elemental weight percentage of filler wire, and the results are given in Table 1. The welding of plates was performed in three different conditions, such as conventional GMAW, SP-GMAW, and DP-GMAW, using the KEMPI GMAW setup (Fig. 1). The full depth of penetration is obtained in the first and second pass.

The following condition was maintained during welding, (i) wire feed rate of 100 mm/s, (ii) argon gas (99.99% pure) flow rate of 15 L/min, and (iii) filler wire diameter of 1.2 mm. The weld pool was protected from the atmospheric oxygen with a sufficient supply of argon gas. The wire brush was utilised for eliminating the impurities or oxide scale present on the weldment after the first pass. The weldment has shown no cracks, as well as defects, and the respective process conditions are displayed in Table 2. The total heat provided (H_T) was calculated by adding the first and second pass heat provided (H_p) for GMAW, SP-GMAW, and DP-GMAW techniques (Table 2). The schematic diagram of the current waveform for all three-welding techniques are displayed in Fig. 2. The value of mean currents is different for GMAW, SP-GMAW, and DP-GMAW techniques which are determined by the following equation (Ref. 18, 28) (Eq. 1-4),

Mean current for GMAW,

$$I_m = I_{mc}(A) \tag{Eq 1}$$

Mean current for SP-GMAW,

$$I_m = I_{m(\text{sp})} = \frac{(I_{p1} \times t_{p1}) + (I_{b1} \times t_{b1})}{t_{p1} + t_{b1}}(A) \tag{Eq 2}$$

Mean current for DP-GMAW,

$$\begin{aligned} I_m &= I_{m(dp)} \\ &= \frac{(I_{p1} \times t_{p1}) + (I_{b1} \times t_{b1}) + (I_{p2} \times t_{p2}) + (I_{b2} \times t_{b2})}{t_{p1} + t_{b1} + t_{p2} + t_{b2}}(A) \end{aligned}$$
$$\tag{Eq 3}$$

The heat provided for each pass is given by,

$$H_p = \frac{V \times I_m}{S} \times \eta \left(\text{kJ}/\text{mm}\right) \tag{Eq 4}$$

where H_p is the heat provided in each pass (kJ/mm), V Voltage (A), I_{mc} mean current of conventional GMAW (A), $I_{m(\text{sp})}$ mean current of SP-GMAW (A), $I_{m(\text{dp})}$ mean current of DP-GMAW, S linear welding speed (mm/s), welding arc efficiency (60%), pulse ON time-50%, pulse OFF time-50%, I_{b1}, I_{p1} base or background current and pulse current during thermal strong cycle (A), I_{b2}, I_{p2} background current and pulse current during thermal weak period (A), t_{b1}, t_{p1} time of base and peak current during thermal strong cycle (s), t_{b2}, t_{p2} time of base and peak current during thermal weak cycle (s).

2.2 Analysis of Microstructure

The non-destructive radiography testing was performed on the weldment to identify defects such as cracks, porosity, inclusion, and other impurities. After testing, the weldments were sliced into different sizes as per the ASTM standard for microstructural characterisation and mechanical testing by W-EDM. The CAD model given in Fig. 3 shows the locations on the welded plate where samples for microstructural investigation were cut out. Samples from the welded plates were mechanically polished using emery sheets of grit size ranging from 220 to 2000, followed by cloth polishing using Al_2O_3 water suspension to take the polished surface to mirror finish. Mechanically polished surfaces were electrolytically etched using an electrolyte having oxalic acid (10 g) and water (100 ml). The etching was done for 8-10 s at 12 V. Dino-lite-edge digital macroscope (model: AM4115T) was used to record the macrostructures of the weldments. The ZEISS optical microscope was used to capture the microstructures from the weld interface (WI) and weld centre (WC) of all the weldments. Analysis of the distribution of various alloying elements from the dendritic core and interdendritic of WI and WC was analysed through a scanning electron microscope (SEM) (model: EVO 18) based EDS (energy dispersive spectroscope) analysis. The BRUKER D8 XRD (x-ray diffraction) machine was used to confirm the secondary precipitates that occurred in the fusion zone. Then, the crystallite size was calculated from XRD results using Scherrer's formulae and gaussian technique. SEM-based EBSD was adopted to analyse the microstructure from the weldments. Samples for EBSD analysis were prepared by mechanical polishing as well as cloth polishing followed by Buehler Vibratory Polisher (Model: Vibromet 2) using colloidal silica suspension. The acquisition of EBSD scans with a step size of 5 μm was performed using a fully automated Aztec HKL Advanced (plus C5 Prem) Nordlys Max 2 EBSD system linked with an FEL SIRION XL30 field-emission gun scanning electron microscope, with an accelerating voltage of 25 kV.

Table 1 Elemental composition of Hastelloy X and ERNiCrMo-2 (filler wire)

Base metal/filler wire	Composition, wt.%										
	Ni	Cr	Fe	Co	Mo	Mn	Si	W	C	P	S
Hastelloy X	Bal	22.33	18.14	0.86	9.15	0.23	0.25	0.20	0.05	0.01	0.001
ERNiCrMo-2 (Filler)	Bal	21.28	19.70	1.35	8.60	0.26	0.44	0.24	0.06	0.01	0.005

Fig. 1 Hastelloy X welded by (a) GMAW-ERNiCrMo-2 (b) SP-GMAW-ERNiCrMo-2 (c) DP-GMAW-ERNiCrMo-2

Table 2 Process parameters of GMAW, SP-GMAW, and DP-GMAW techniques

Welding technique	Name of pass	Input current, A		Input voltage (V), V	Welding speed (S), mm/s	Heat input in each pass (H_p), kJ/mm	Total heat input, (H_T), kJ/mm
		I	I_m				
GMAW	First	I_c 130	130	21.7	2.250	0.752	0.842
	Second	I_c 130	130	21.7	18.889	0.090	
SP-GMAW	First	I_{p1} 130 I_{b1} 65	97.5	21.7	2.250	0.564	0.631
	Second	I_{p1} 130 I_{b1} 65	97.5	21.7	18.889	0.067	
DP-GMAW	First	I_{p1} 130 I_{b1} 65 I_{p2} 97.5 I_{b2} 48.75	85.3	21.7	2.250	0.494	0.553
	Second	I_{p1} 130 I_{b1} 65 I_{p2} 97.5 I_{b2} 48.75	85.3	21.7	18.889	0.059	

HKL Channel 5 software of Oxford instrument was used to process EBSD maps for this study.

2.3 Evaluation of Mechanical properties

Based on the ASTM standard (E8/E-8 M-13a), the tensile samples were prepared from the weldment perpendicular to
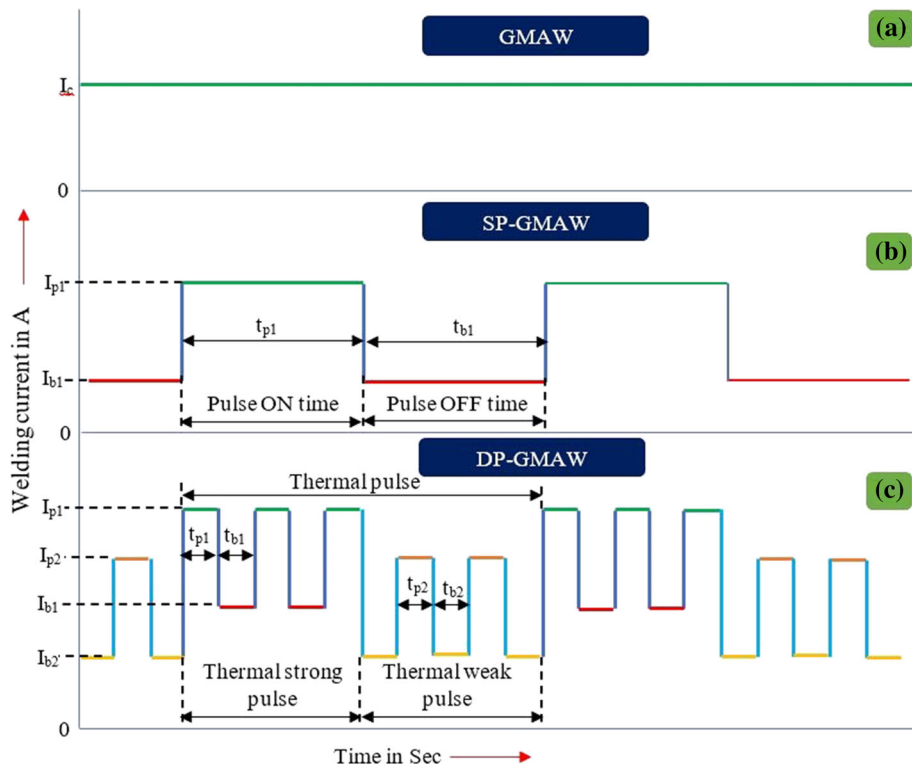
Fig. 2 Current waveform of (a) GMAW technique (b) SP-GMAW technique (c) DP-GMAW technique

welding direction (transverse) for determining the important mechanical properties like the total percentage of ductility, 0.2% proof stress (PS), and ultimate tensile strength (UTS) of all the weldments. Three samples per condition were evaluated at a strain rate of 2 mm/min using servo-hydraulic Instron (Model: 8801 machines fitted with 100 kN load cell). Samples were tested at room temperature and taken up to fracture. Samples for the Charpy impact test were prepared as per the ASTM standard (E23-04) with the V-notch angle of 45° and depth of 2 mm. The FIT 300-O pendulum toughness testing equipment was used to perform Charpy the impact toughness of the weldment at room temperature. CAD model showing the scheme used for extracting the samples for mechanical tests and microstructural analysis is shown in Fig. 3. For both impact and tensile testing, three samples per condition were tested to ensure repeatability. The resistance to deformation occurring during the indentation process of base metal, WC, and WI was measured through the Vicker's microhardness testing machine with a diamond indenter (ASTM E384-17). The testing was done at 500 gf load, 0.25 mm interval for 10 s at room temperature.

3. Results

3.1 Macrostructure

The weld defects, such as porosity, inclusion, and other impurities in weldment, are evaluated through the macrostructure analysis. The cross-sectional weld bead profiles of GMAW, SP-GMAW, and DP-GMAW weldments are displayed in Fig. 4(a-c). The weldment showed defect-free welding in all three conditions. The weld bead width (top and bottom) of the

GMAW weldment is higher than SP-GMAW and DP-GMAW. The lowest top width to depth of penetration ratio is observed for DP-GMAW (1.455), followed by SP-GMAW (1.544) and GMAW (1.634) weldment.

3.2 Microstructure

The optical micrographs of base metal, GMAW, SP-GMAW, and DP-GMAW are displayed in Fig. 5(a-f). The austenitic structure is observed in face centred cubic (FCC) matrix, and annealing twin boundaries are also observed in some regions. The cellular structure is also clearly revealed in the weld centre of weldment made by the GMAW technique (Fig. 5(a)). Whereas equiaxed dendrites are identified in the weld centre of SP-GMAW (Fig. 5(c)) and DP-GMAW (Fig. 5(e)). The optical micrographs of all the weldments are showing the evidence for the development of the columnar structure at the weld interface (WI) (Fig. 5b, d, f). The weldment made by the DP-GMAW technique showed a narrow heat-affected zone (HAZ) as compared to that of weldment made by SP-GMAW and GMAW techniques.

3.3 Microsegregation

The SEM micrographs recorded at two different magnifications (3000X and 10000X) from both weld centre as well as weld interface of three weldments (GMAW, SP-GMAW, DP-GMAW) are given in Figs. 6, 7, and 8, respectively. The formations of secondary precipitates are visible at higher magnification micrographs, and the elemental composition at the dendritic and interdendritic region is analysed through SEM-based EDS analysis. The EDS measurement of the elemental peaks is presented in Figs. 6, 7, 8 (i-iv) for GMAW, SP-GMAW, and DP-GMAW, respectively. The segregation of
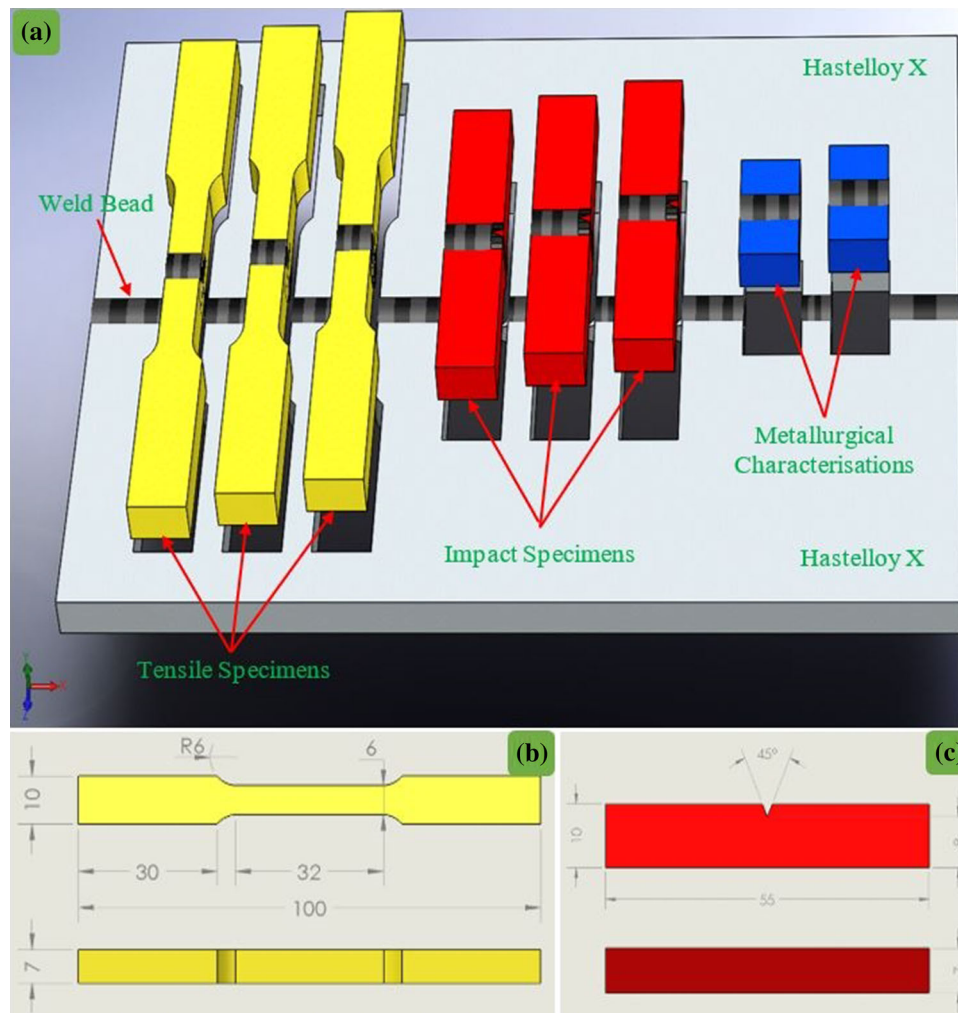
Fig. 3 (a) CAD model illustrating the location and orientation of samples extracted from the 7 mm thick welded plate for mechanical tests and microstructural analysis; (b) geometry and dimensions of samples used for (b) tensile specimen and (c) impact specimen

the Cr element is completely precluded for all the weldments. EDS analysis confirmed the formation of Mo-rich in the interdendritic region of GMAW weldment at both WI and WC (Fig. 6 (i-iv)). But, the segregation of Mo-rich precipitates is reduced for the case of SP-GMAW weldment due to the pulsing of input current (Fig. 7 (i-iv)). The occurrence of Mo-rich segregation is completely precluded in DP-GMAW (Fig. 8 (i-iv)). The EDS line mapping drawn across the interdendritic region and the peaks of different elements for WC and WI are presented in Figs. 9, 10, 11, 12, 13, and 14. Further, Figs. 9 and 10 inveterate the formation of Mo-rich precipitates in WC and WI of GMAW. Similarly, evidence for the formation of Mo-precipitates in the weldment was obtained by the SP-GMAW technique (Figs. 11, 12). In contrast to the above result, in DP-GMAW, the peaks of Mo-rich precipitates are not observed in both WC and WI regions (Figs. 13, 14). The observed EDS compositions are compared with EDS line mapping and results showing similar effects.

3.4 Phase Analysis

The precipitates in the weldments are determined through XRD peaks. Figure 15 reports the precipitates observed in GMAW, SP-GMAW, and DP-GMAW. The existence of M_3C

(Fe_2MoC) and M_6C (Fe_2Mo_4C) is found in both GMAW and SP-GMAW. This is due to the segregation of Mo at the interdendritic region of GMAW and SP-GMAW. Further, DP-GMAW reports only Mo_1Ni_4 precipitates. Besides, the mean grain size is evaluated through Scherrer's formula, and it is given below (Ref. 29) (Eq. 5). Mean grain size is given by

$$d = \frac{k\lambda}{\beta \cos \theta} \text{ in nm} \tag{Eq 5}$$

where λ is equal to 1.54 θ $\times$ 10^{-10} m (wavelength of x-ray), d is mean grain size in nm, β is full width half maximum (FWHM) intensity in radiant, θ is the angle of diffraction in degree, and k is equal to 0.94 (shape factor).

3.5 Tensile Properties

Dog bone-shaped tensile samples machined out from the welded plates by adopting three different techniques are subjected to tensile tests at room temperature to determine properties like ultimate tensile strength (UTS), mean % of elongation (Ductility), and mean 0.2% of proof stress (PS). Three samples per condition were tested and compared with that of base metal (Table 3). Photographs showing tensile tested samples from all tested conditions are given in Fig. 16(a-c).
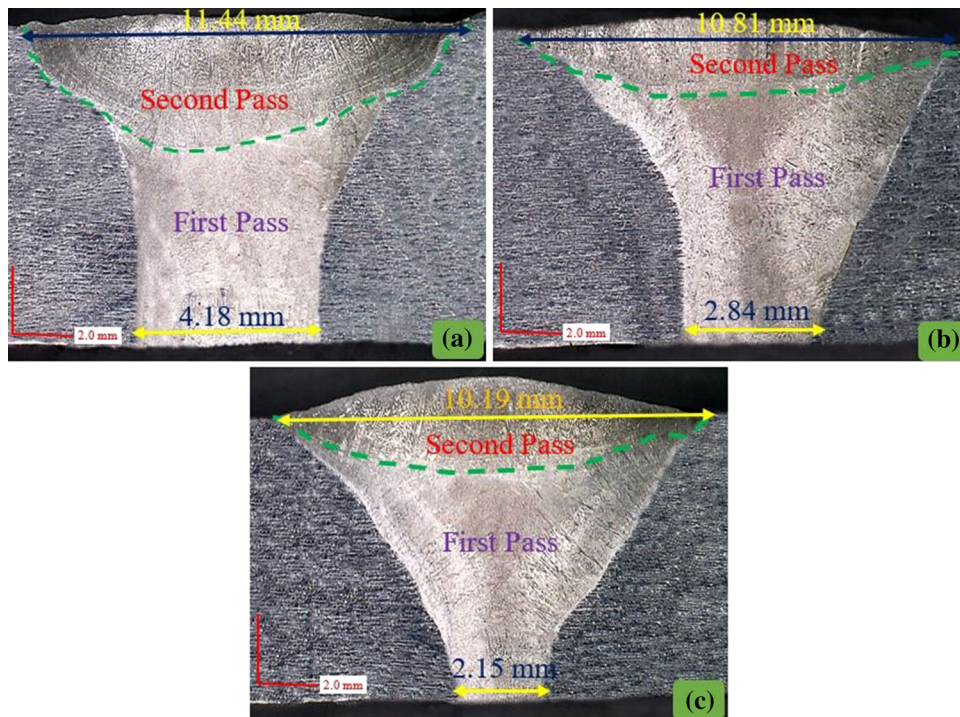
Fig. 4 Macrostructure of Hastelloy X welded by (a) GMAW-ERNiCrMo-2, (b) SP-GMAW-ERNiCrMo-2, and (c) DP-GMAW-ERNiCrMo-2

Noticeable difference in the way of the fracture occurred in the tested samples of each condition after localised necking is observed in the photograph showing the close-up view of fractured tips (Fig. 16 (i-ix)). The samples representing base metal conditions provide the highest UTS as well as ductility compared to all three weldments. The UTSs observed in DP-GMAW are significantly higher (10.61%, 21.96%) than SP-GMAW, and GMAW condition. Similarly, DP-GMAW provides a better ductility of 48% and 131.25% than SP-GMAW and GMAW, respectively. Differences in the microstructural characteristics of the weld centre and weld interface played a role in influencing the tensile behaviour of samples from three conditions.

3.6 Microhardness

The microhardness of base metal, GMAW, SP-GMAW, and DP-GMAW is measured at the different locations, and results are plotted with respect to distance from weld centre verses Vicker's microhardness which is displayed in Fig. 17. The base metal revealed the mean microhardness of 231.1 ± 4.9 HV. From the plot, it is found that DP-GMAW (226.0 ± 3.6 HV) is delivering a slightly higher mean microhardness than GMAW (210.6 ± 5.4 HV), and SP-GMAW (218.3 ± 4.0 HV).

3.7 Impact Toughness

The mean impact energy absorbed by base metal, GMAW, SP-GMAW, and DP-GMAW are determined through the impact toughness analysis. Three samples are tested in each case to obtain better conclusions, and the values are given in Table 4. Before fracture, DP-GMAW is absorbed higher energy compared to GMAW, and SP-GMAW. DP-GMAW provides 49.01%, 26.67% higher energy than GMAW, SP-GMAW.

3.8 EBSD Analysis

From the above results, it is clear that SP-GMAW and DP-GMAW are giving better results when compared to GMAW. So, the EBSD analysis is only performed on SP-GMAW and DP-GMAW for obtaining in-depth material characterisation. Inverse pole figure (IPF) and Euler maps of the base metal (Hastelloy X), SP-GMAW, and DP-GMAW are displayed in Fig. 18(a-f). The grain orientation spread (GOS) and recrystallisation fraction maps are given in Fig. 19(a-f). Further pole figures of base metals and weldments are displayed in Fig. 20(a-c). The orientation distribution fractions (ODF) of base metal, SP-GMAW, DP-GMAW, and FCC standard ODF at different $\phi_2 = 45°$ sections of Euler space is shown in Fig. 20(a-d).

4. Discussion

4.1 Bead Quality

The quality of the weld bead can be explained by a different mode of transfer observed during welding (Fig. 4(a-c)). As pointed out from the micrographs that no micro-cracks are observed for GMAW, SP-GMAW, and DP-GMAW methods. The width of the weld bead is primarily explained by mode of transfer and amount of heat supplied. The spray mode of transfer is observed for conventional GMAW due to the high current supply. During GMAW, the pinch forces are sufficient enough to detach the molten droplets from the torch, and many numbers of droplets are observed in the gap between torch and weld plate. This will lead to spatters and collision of droplets whilst travelling. In the case of single pulse (SP-GMAW) condition, the droplet mode of transfer is observed, and during
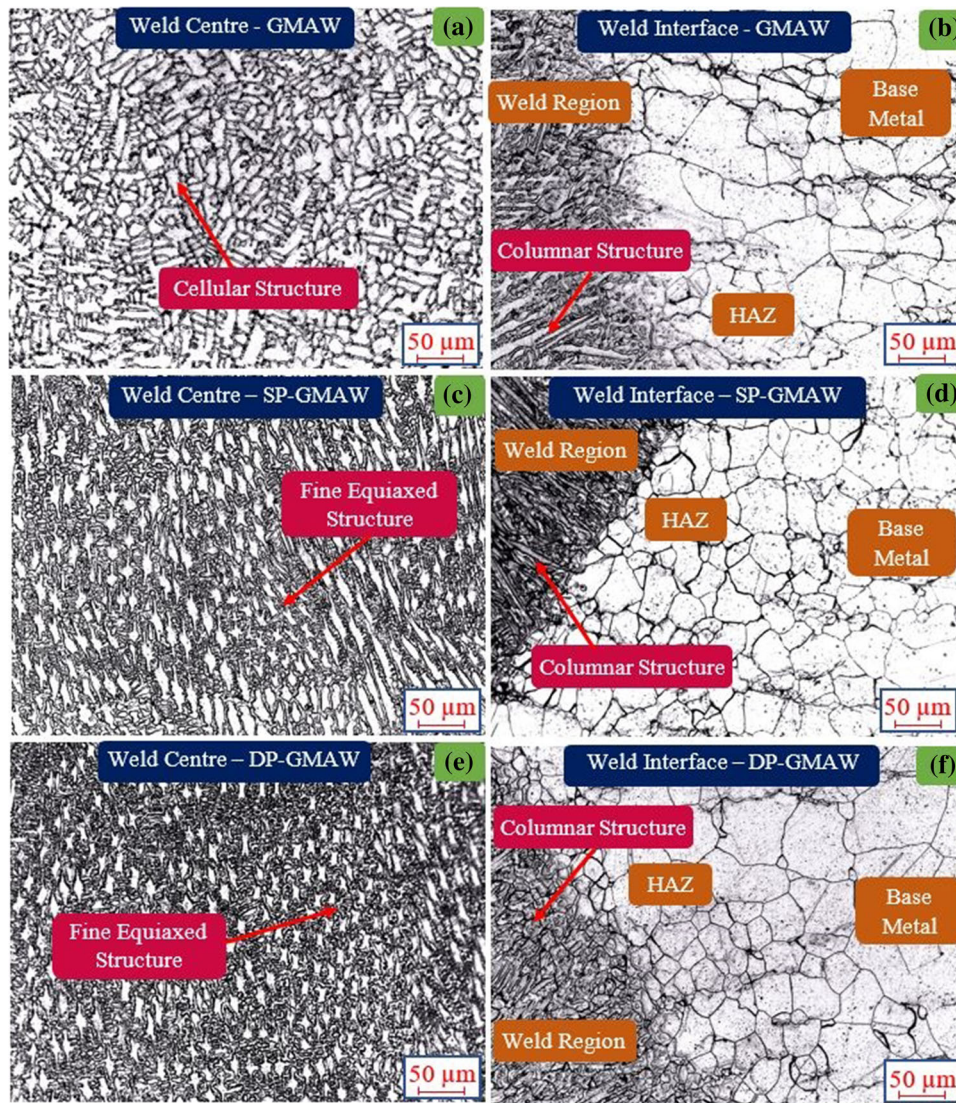
Fig. 5 Microstructure of Hastelloy X welded by (a) GMAW-WC, (b) GMAW-WI, (c) SP-GMAW-WC, (d) SP-GMAW-WI, (e) DP-GMAW-WC, and (f) DP-GMAW-WI

pulse ON condition, the filler wire is heated and melted. Finally, droplets are formed which is transferred to the workpiece with the help of pinch force and gravitational force (Ref. 24, 30). During pulse OFF condition, filler wires are not heated, and droplets which transferred to the workpiece during pulse ON period gets solidified. In this mode, one droplet is transferred during one cycle (pulse ON and pulse OFF). In case of double pulse (DP-GMAW) condition, the high-frequency pulse (HFP) and thermal pulse frequency are simultaneously used during welding. The base and peak value of HFP are cyclically varied during thermal pulse fluctuation (Ref. 25, 26), and its main role is to ensure the behaviour of the droplet transferred (one droplet per pulse) and to sustain the arc stability during welding. The thermal pulse is used to control the HFP duration, which improves the weld pool stirring, ensures the formation of the weld pool ripple (Ref. 31). These mechanisms are primarily attributed to the weld pool volume, size, and shapes. Thus, results in low weld pool width in DP-GMAW compared to SP-GMAW and GMAW (Fig. 4(a-c)).

4.2 Microstructure

The microstructural changes of weldments at the weld centre and weld interface region for GMAW, SP-GMAW, and DP-GMAW are illustrated in Fig. 5(a-f). Besides, the columnar dendrites are propagated through the direction of heat extraction, and it is mainly developed by the directional growth of new nuclei and dendrite growth. The existence of columnar dendrite, and fine equiaxed structure, mainly depends on the constitutional supercooling (Ref. 20, 32). The high rate of constitutional supercooling observed in DP-GMAW, followed by SP-GMAW, causes the fine equiaxed dendrites (Ref. 25, 31, 33). Whereas the low rate of constitutional supercooling promotes the cellular dendrites in GMAW weldment. Further, the development of new dendrites is reported by the heterogeneous nucleation, dendrite refinement or fragmentation, and dendrite detachment mechanisms. The high cooling rate in DP-GMAW reduces the solidification time, which guides the severe heterogeneous nucleation, larger grain refinement, and detachment. This concludes the finer grains during DP-GMAW, and
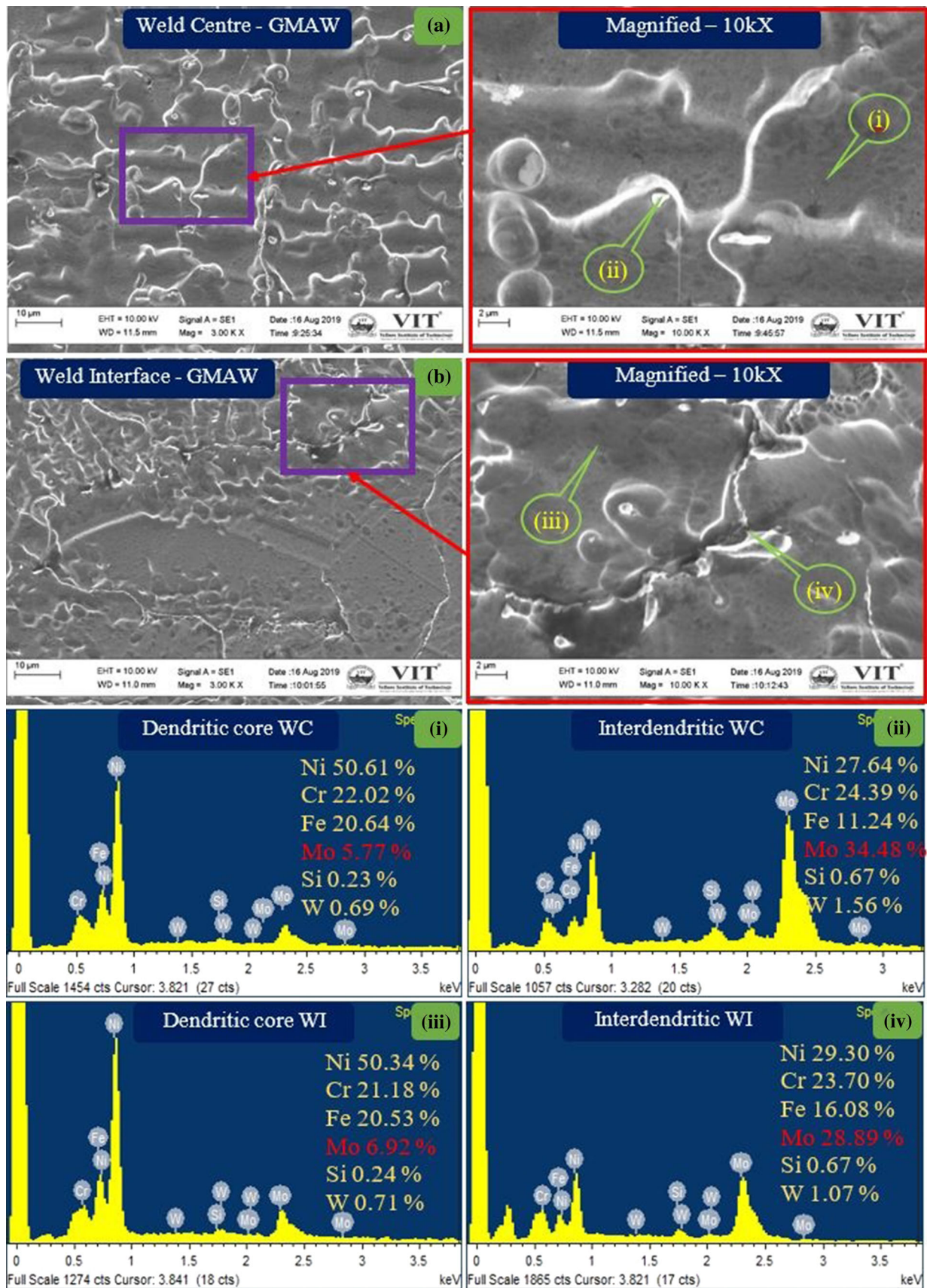
Fig. 6 SEM images of Hastelloy X welded by (a) GMAW-WC (b) GMAW-WI (i) EDS-Dendritic core of WC (ii) EDS-Interdendritic of WC (iii) EDS-Dendritic core of WI (iv) EDS-Interdendritic of WI
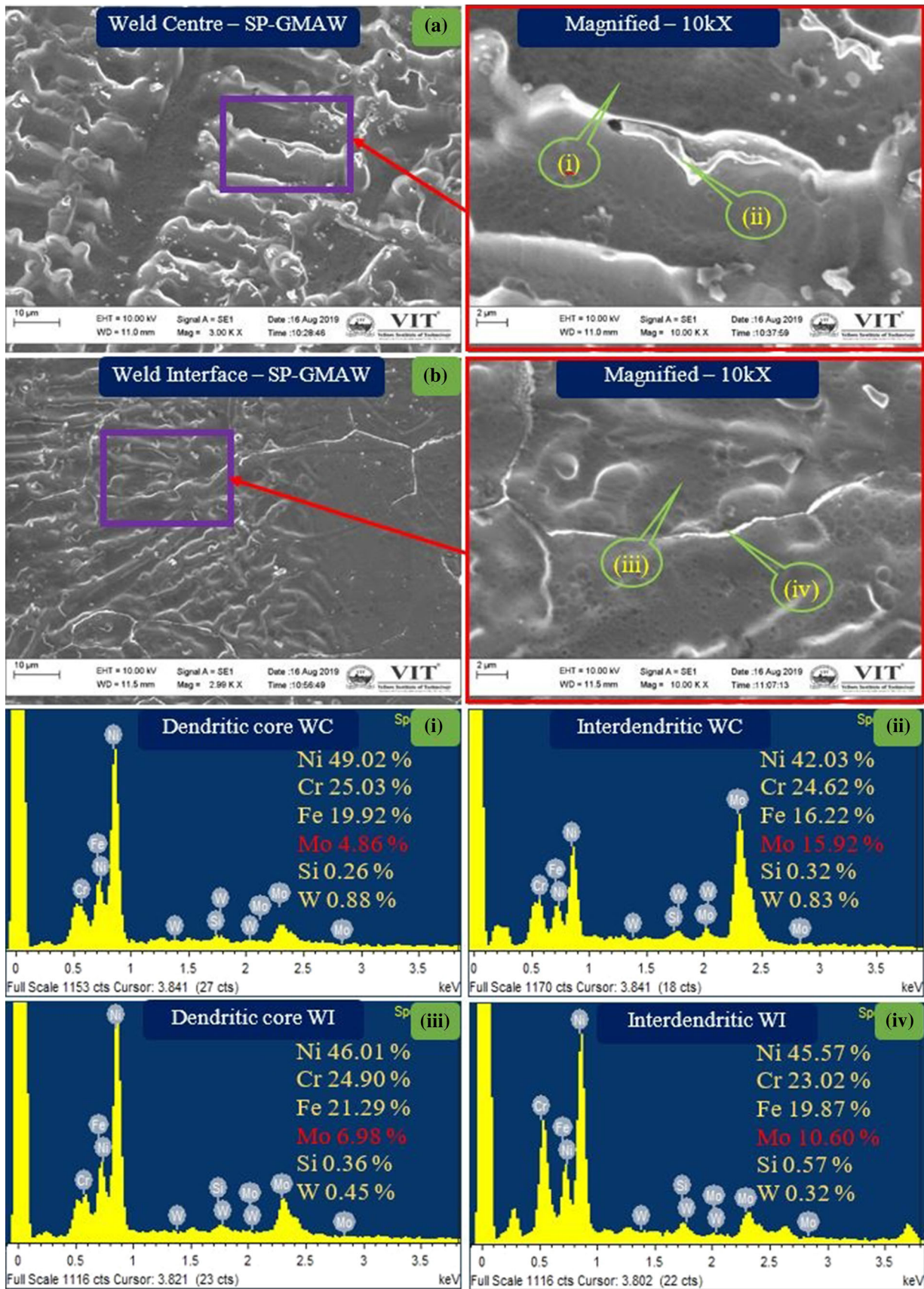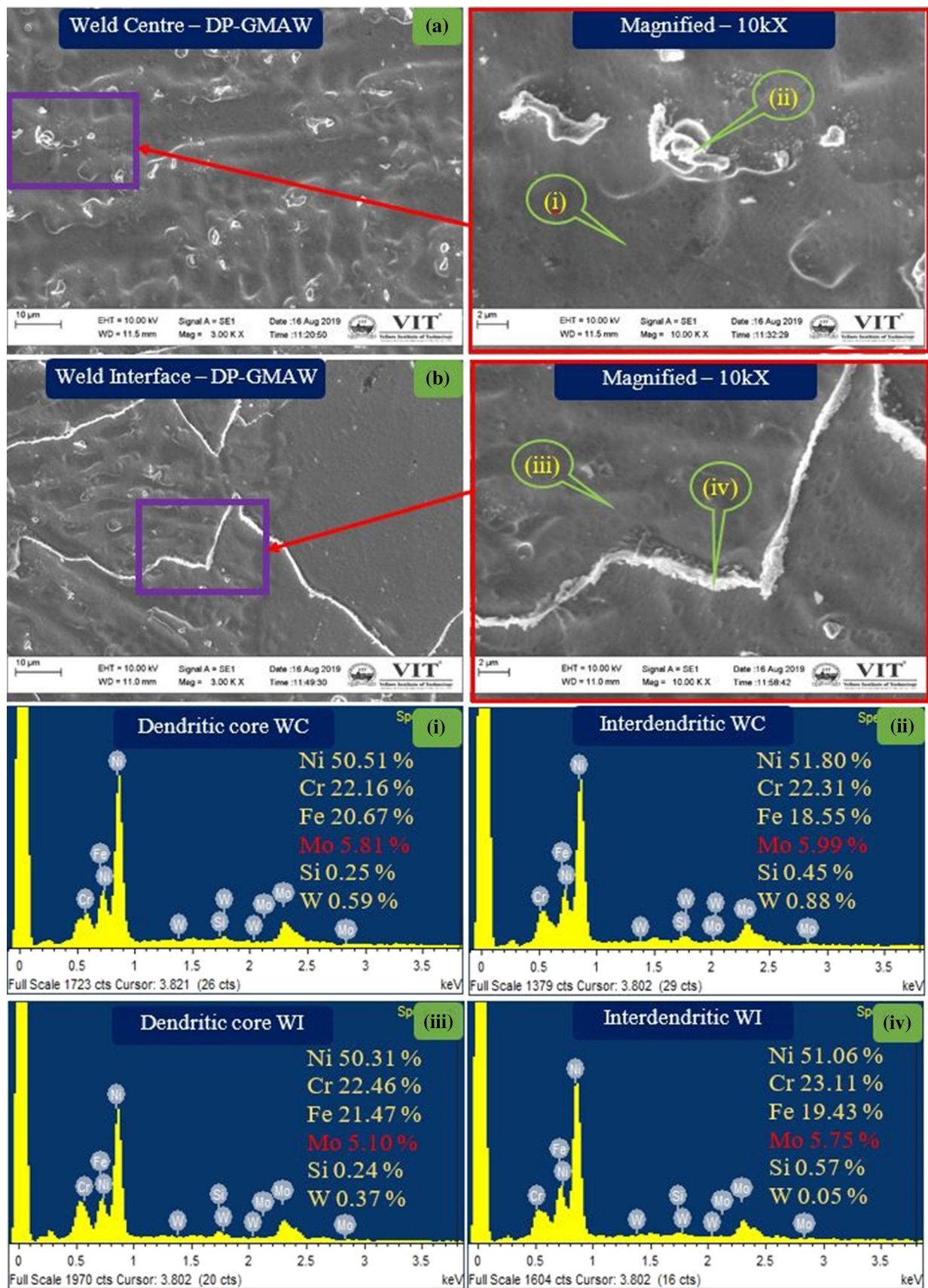
Fig. 7 SEM images of Hastelloy X joined with (a) SP-GMAW-WC (b) SP-GMAW-WI (i) EDS-Dendritic core of WC (ii) EDS-Interdendritic of WC (iii) EDS-Dendritic core of WI (iv) EDS-Interdendritic of WI

Fig. 8 SEM images of Hastelloy X joined with (a) DP-GMAW-WC (b) DP-GMAW-WI (i) EDS-Dendritic core of WC (ii) EDS-Interdendritic of WC (iii) EDS-Dendritic core of WI (iv) EDS-Interdendritic of WI
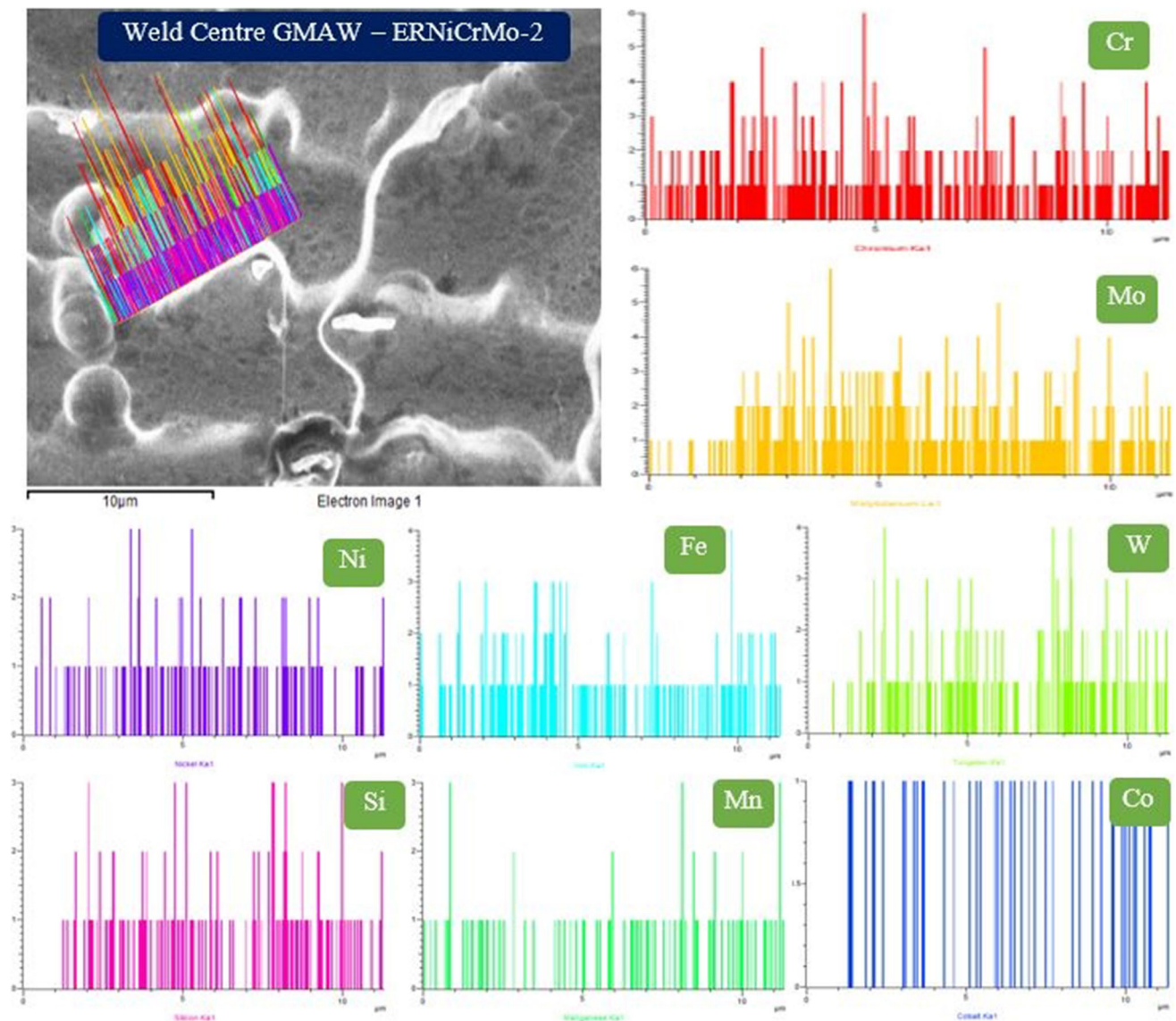
Fig. 9 EDS line mapping of Hastelloy X welded by GMAW-ERNiCrMo-2 at weld centre

SP-GMAW also causes the same effect. Whereas the slow cooling rate observed in GMAW increases the solidification time that lower down the heterogenous nucleation and causes coarser grains. Besides, the microstructural changes are identified by thermal gradient (G) and grain growth rate (R). The product of GR used to evaluate the grain size, and the ratio of G/R delivers the type of solidification (Ref. 19, 22, 23, 34). At the weld centre, G/R ratio is low compared to the fusion boundary. Hence, it is clear that the ratio keeps on decreases as moved towards the weld centre. This results in the different dendritic structures at the weld centre and interface. Therefore, high GR found in DP-GMAW reduces the grain size compared to SP-GMAW and GMAW (Ref. 35). Further, Rosenthal three-dimensional equation is useful in evaluating the heat circulation and temperature distribution over the weldment based on the welding speed and heat supply. The relationship of grain size with different heat input and cooling rates observed in DP-GMAW, SP-GMAW, and GMAW are explained with Rosenthal equation (Ref. 27) (Eq. 6).

$$\frac{2(T - T_o)kR}{Q} = \exp\frac{-V(R - x)}{2\alpha} \qquad \text{(Eq 6)}$$

where R radial distance to heat source; T temperature; T_o Initial temperature; Q heat transferred to the workpiece; V travelling speed; k thermal conductivity of base metal; α thermal diffusivity of the workpiece.

Based on this equation, the cooling rate increases as the ratio of heat supply to travelling speed (Q/V) decreases. Therefore, a high cooling rate in DP-GMAW makes refined grains (Ref. 24) and lower intergranular spacing compared to SP-GMAW and GMAW (Ref. 27). During the welding of Hastelloy X, the liquation cracks are formed over the HAZ region (Ref. 13, 36). This results in a tremendous reduction in the mechanical properties of the weldment. In this study, such cracks are not observed for all three welding conditions. Based on this, the width of HAZ also plays an important role in determining the quality of weldments. Hence the better fluid flow, higher thermal gradient, rapid cooling rate, a lower ratio of Q/V, higher
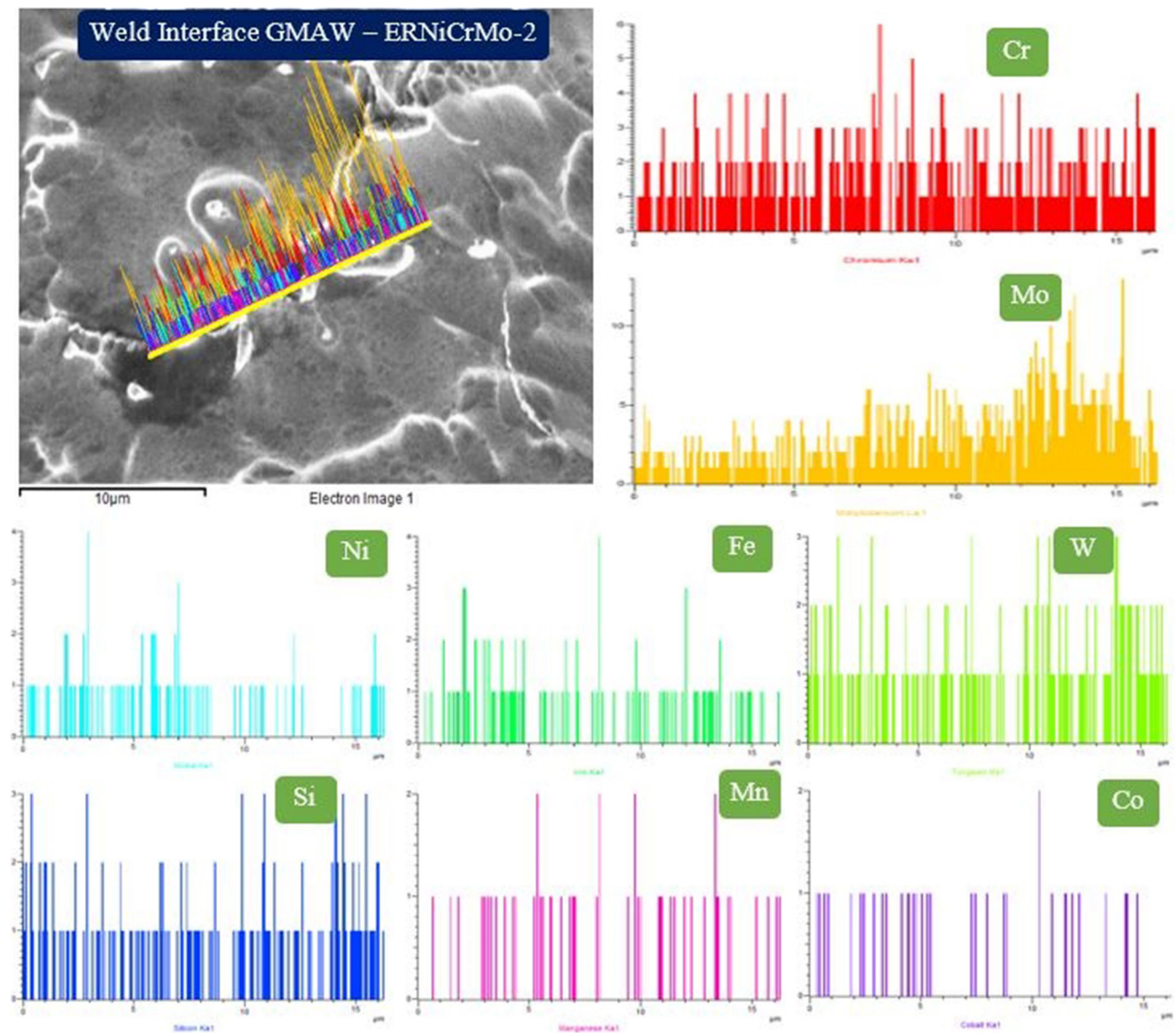
Fig. 10 EDS line mapping of Hastelloy X welded by GMAW-ERNiCrMo-2 at weld interface

product of GR observed in DP-GMAW are primarily attributed to lower HAZ width compared to SP-GMAW and GMAW.

4.3 Microsegregation

The SEM photographs with 10kX magnification pointed out the existence of precipitates at the interdendritic zone for GMAW, SP-GMAW, and DP-GMAW, respectively. The differences are illustrated in Fig. 6-8 (i-iv). The morphologies of carbide precipitates and micro-crack in the weldments are observed through SEM photographs. The photographs show the absence of micro-cracks in both HAZ and WZ. The M_6C is identified in the form of coarse cubic, script shapes, and acicular form with face centred cubic structure, whereas M_3C observed in the orthorhombic structure. Development of these carbides mainly depends on the Mo-rich segregation during welding. In SP-GMAW, Mo-rich segregation is reduced whereas, in DP-GMAW, the formation of these precipitates are completely precluded due to the existence of refined grain size, which has a higher grain boundary area due to low free

energy. It results in the preclusion of carbide precipitates around the grain boundaries. Whereas in GMAW, the developments of secondary carbides are increased due to coarser grain, which improves grain boundary area due to high free energy. It results in increased carbide precipitates around the grain boundaries. Other researchers also pointed out the similar kind of observation (Ref. 21, 37).

The EDS results are used to find out the elemental weight percentage in the dendritic core and interdendritic zone. EDS results of GMAW, SP-GMAW, and DP-GMAW are displayed in Figs. 6, 7, and 8 (i-iv), respectively. As concluded from the graph, Cr segregation is precluded completely for all three welding conditions. The severe Mo-rich segregation is found in the interdendritic zone of GMAW at WI and WC (Fig. 6 (i-iv)). The supply of high heat decreases the cooling speed and thermal gradient that increases the solidification period after welding. This provides the required time for Mo-rich elements to segregate at the interdendritic region. The development of Mo-rich elements in the interdendritic place reduces the properties of the material by giving easy nucleation sites for
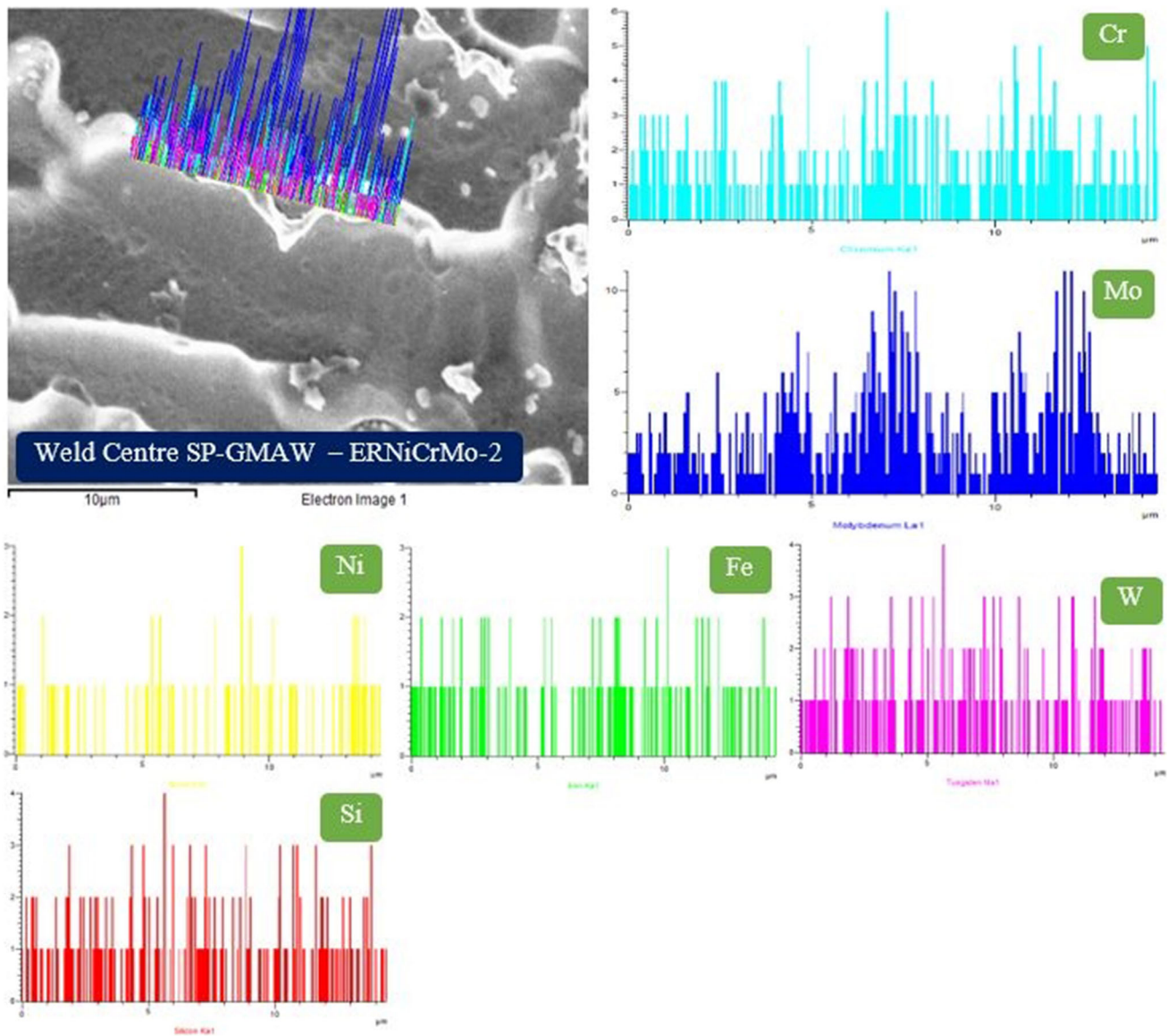
Fig. 11 EDS line mapping of Hastelloy X welded by SP-GMAW-ERNiCrMo-2 at weld centre

the crack to grow. Further, it is also pointed out from the results that Mo-rich segregation is minimum for SP-GMAW. This is primarily attributed by the pulsing current (pulse ON and pulse OFF) supplied during welding. Hence, total heat input is reduced in SP-GMAW, which promotes the rapid cooling, high thermal gradient, and lower solidification time. It does not provide a sufficient period for Mo elements to segregate in the interdendritic region (Fig. 7 (i-iv)). But Mo segregation is completely absent for DP-GMAW condition. The combination of HFP and thermal pulse frequency supplied during welding results in rapid cooling, very high thermal gradient, and very low solidification time, in comparison with GMAW and SP-GMAW. Therefore, very low solidification time observed in DP-GMAW completely precludes the Mo-segregation (Fig. 8 (i-iv)). Consequently, the EDS line mapping is drawn over the interdendritic region in order to confirm the segregation of Mo elements at both WC and WI. The dominant peaks of Mo-rich elements are observed for GMAW and SP-GMAW weldment compared to other elements like Ni, Fe, Cr, W, and Si (Fig. 9-12). Whereas in DP-GMAW, the Ni element shows the

dominant peaks when compared to other elements that confirm the absence of Cr and Mo segregation (Figs. 13, 14). The peaks of line mapping and EDS elemental weight percentages are showing a similar trend.

4.4 Phase Analysis

The XRD reports are used to characterise the precipitates in the weldments made by GMAW, SP-GMAW, and DP-GMAW. The XRD peaks of weldments are displayed in Fig. 15. The XRD reports have confirmed the absence of Cr-rich elements in all three weldments, and it is in-line with EDS analysis. It also displays the occurrence of M_3C (Fe_2MoC), and M_6C (Fe_2Mo_4C) precipitates in both GMAW and SP-GMAW. The severe segregation of Mo-rich elements viewed at the inter-dendritic zone is primarily attributed to these precipitates in the weldment. The development of M_3C (Fe_2MoC) and M_6C (Fe_2Mo_4C) precipitates was reported by other researchers (Ref. 14, 15, 21, 38). These precipitates are formed in the shape of script shapes, coarse cubic, an acicular form, which makes
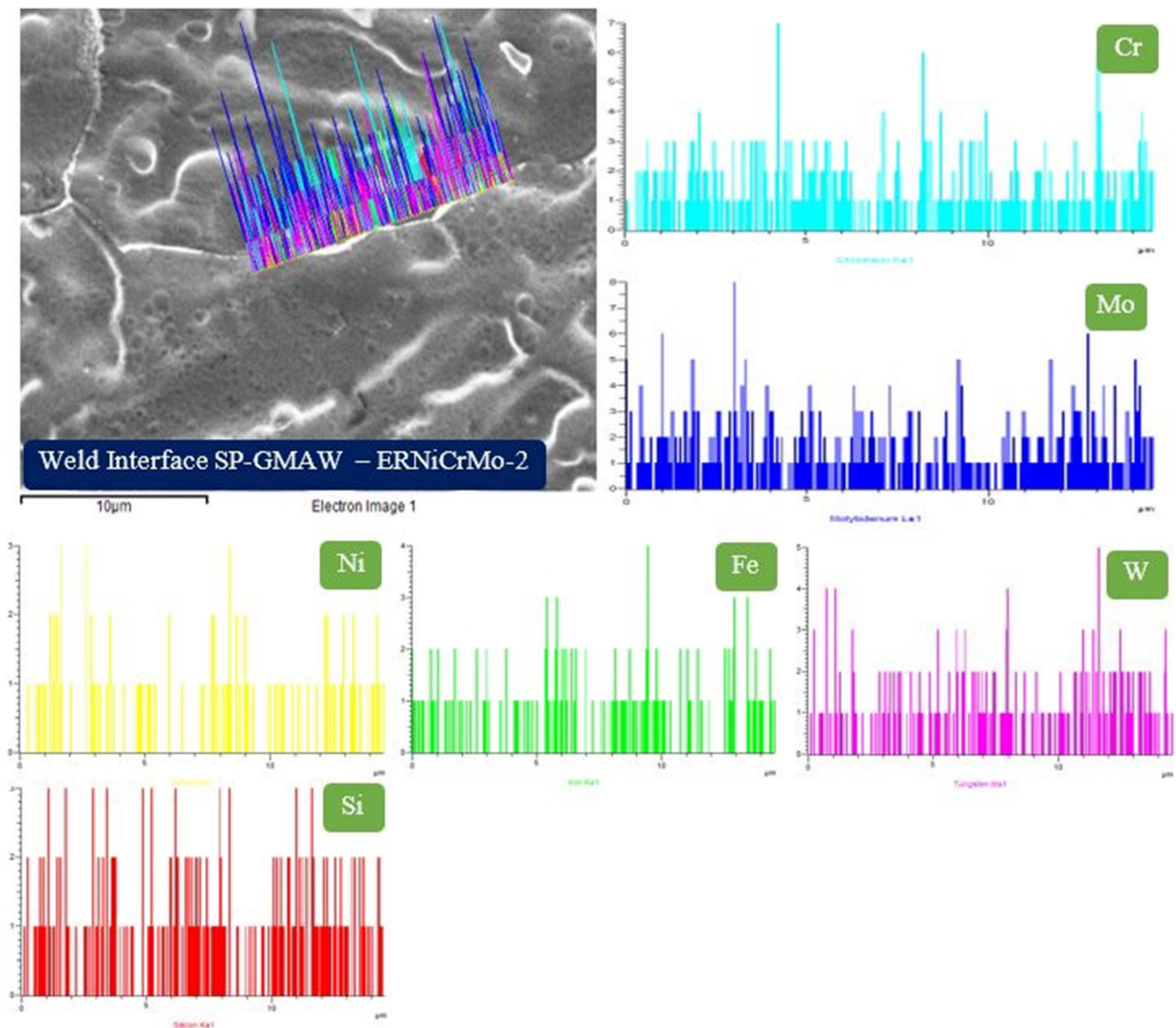
Fig. 12 EDS line mapping of Hastelloy X welded by SP-GMAW-ERNiCrMo-2 at weld interface

weldment to fail easily and results in degradation of mechanical properties. But DP-GMAW only displays the existence of Mo_1Ni_{4-} precipitates that provide sufficient strength to weldment. Hence, in DP-GMAW, the segregation of carbide precipitate is not observed, and the result is in-line with elemental weight percentage observed through EDS reports. Further, the crystalline grain size in the weldment of GMAW, SP-GMAW, and DP-GMAW are measured using Scherrer's equations (Eq. 5). The crystallite grain size of DP-GMAW (18.53 nm) is smaller compared to SP-GMAW (25.39 nm) and GMAW (37.38 nm) techniques. Sathishkumar et al. (Ref. 21) pointed out a similar kind of refined crystallite size in pulsed current welding.

4.5 Tensile Properties

The important tensile properties have pointed out that DP-GMAW is better compared to SP-GMAW and GMAW techniques. Table 3 displays an average PS, UTS, and ductility

of weldments, and it also reveals the region of failure. It is concluded from Fig. 16 that all the weldments are ruptured at WC. This further confirmed that the strength of the weld joint is inferior in comparison with Hastelloy X (base metal) strength. The tensile results show the same trend as microhardness. The inferior microhardness of weldment further confirms that the WC rupture during tensile testing (Ref. 20). The DP-GMAW reveals the highest UTS, and it is followed by SP-GMAW and GMAW. The developments of fine equiaxed dendrite with smaller crystallite grain size along with Mo_1Ni_4 precipitates are primarily attributed to the better strength in DP-GMAW (Ref. 25). Amongst the three weldments, GMAW displays the lower UTS. This is due to the existence of cellular structure in the weldment with larger crystallite grain size when compared to DP-GMAW and SP-GMAW. Besides, the existence of M_3C (Fe_2MoC) and M_6C (Fe_2Mo_4C) precipitates also reduces the tensile strength and ductility of weldments. A similar trend is reported by other researchers (Ref. 13, 14, 39). The ductility of all three weldments is inferior to the base metal. The absence of
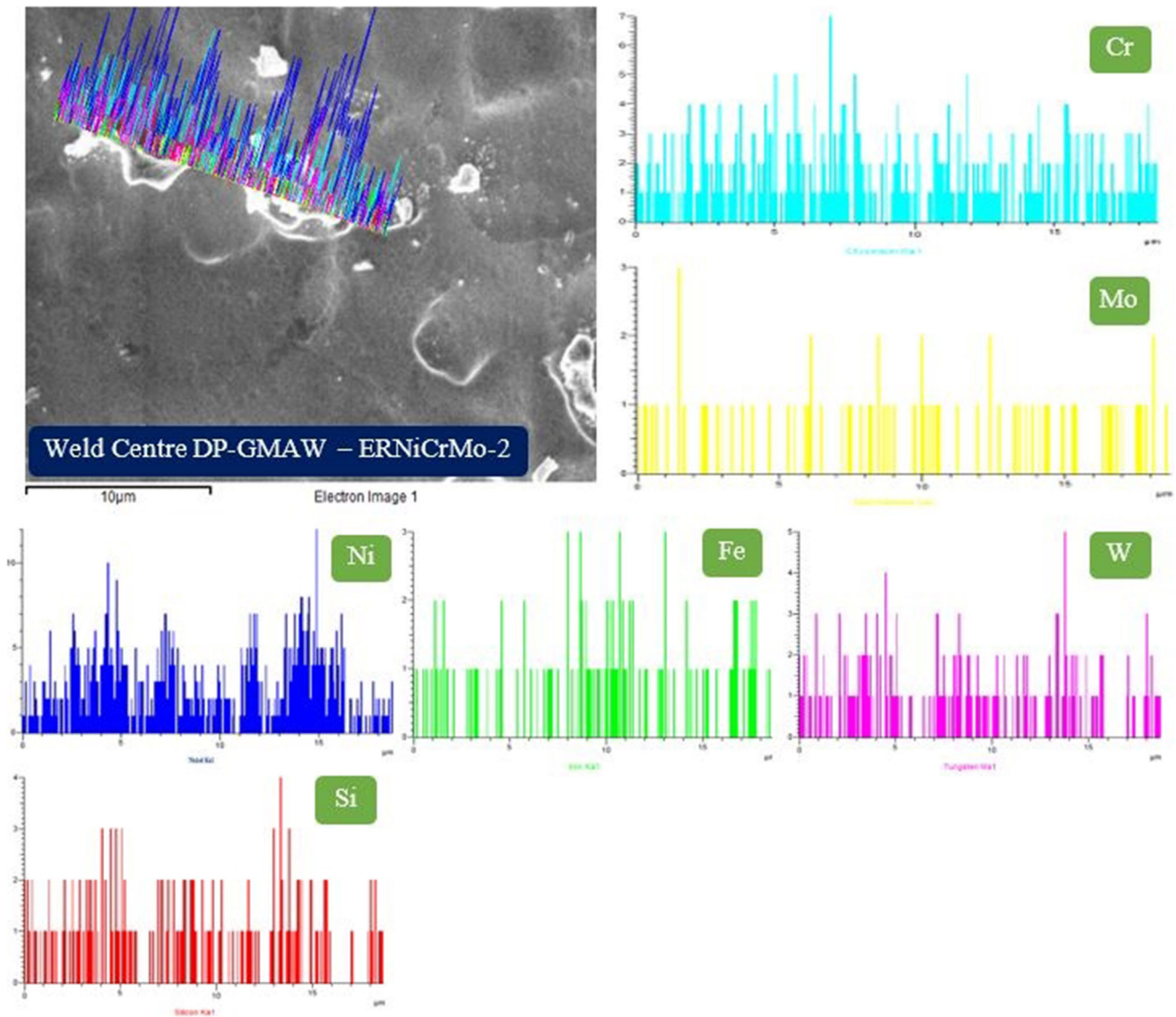
Fig. 13 EDS line mapping of Hastelloy X welded by DP-GMAW-ERNiCrMo-2 at weld centre

carbide precipitates in DP-GMAW provides a higher ductility compared to SP-GMAW and GMAW techniques. The ductility results pointed out the ductile failure in GMAW, SP-GMAW, and DP-GMAW techniques. Further, the joint efficiency is evaluated based on the ratio of UTS of the base metal to weldment, for determining the best weld amongst GMAW, SP-GMAW, and DP-GMAW techniques. The DP-GMAW provides the best joint efficiency of 96.32%, and it is followed by SP-GMAW of 87.08% and GMAW of 78.98%. Therefore, from the tensile study, it is concluded that the GMAW is not suitable for the welding of Hastelloy X whereas DP-GMAW is recommended.

4.6 Microhardness

The microhardness in the different zones of GMAW, SP-GMAW, and DP-GMAW is plotted in Fig. 17. At some points in the microhardness, plots display a much higher value than the previous points. This is due to the indentation on the single

precipitate by indenter, which had better microhardness. Further, it is clear from the microhardness plot that the weld centre (WC) shows a little variation in microhardness values. Apart from that, the base metal shows better microhardness value when compared to all three weldments. In order to opt the best amongst three weldments, the mean or cumulative microhardness values are determined for GMAW, SP-GMAW, and DP-GMAW techniques (Ref. 19). The cumulative micro-hardness values for weldment from three techniques are listed in Table 4. It is noticed that weldment obtained using DP-GMAW technique is showing 7.31% and 3.52% higher microhardness when compared to GMAW and SP-GMAW, respectively. Kaiyun Wu et al. (Ref. 27) also reported a similar observation in the case of mild steel. The development of finer grain size and the absence of carbide precipitates at the interdendritic region are prime factors contributing to the higher microhardness values in the weldment by DP-GMAW. Besides that, the combined effect of thermal pulse and pulsed current could also the reason for higher microhardness (Ref. 25). But
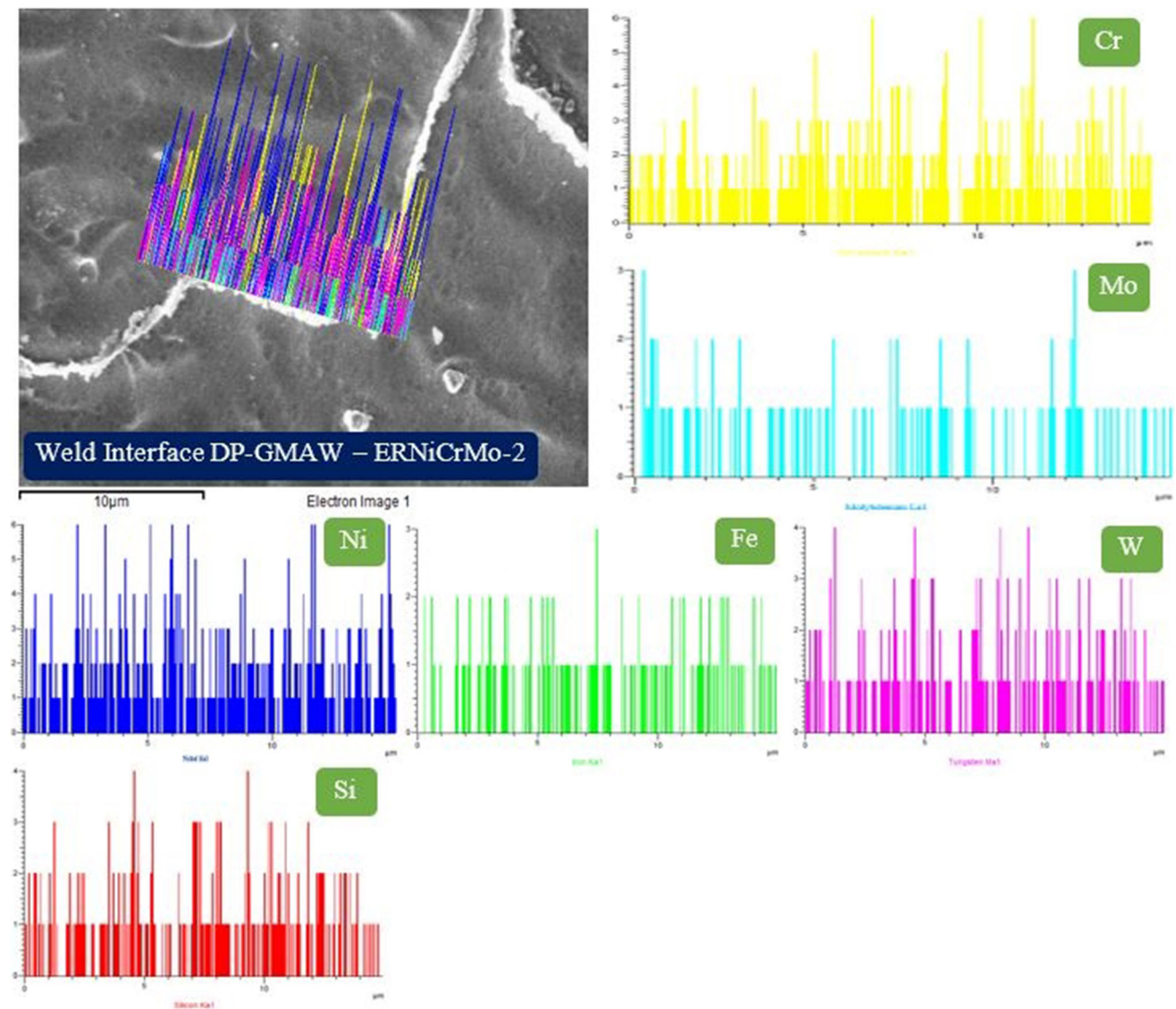
Fig. 14 EDS line mapping of Hastelloy X welded by DP-GMAW-ERNiCrMo-2 at weld interface

the coarser grain size observed in GMAW and SP-GMAW reduces the microhardness.

4.7 Impact Toughness

The energy observed by the weldments after sudden fracture is determined through the impact testing using Charpy V-notch samples. The impact toughness of the base metal, as well as weldments, made using GMAW, SP-GMAW, and DP-GMAW techniques are listed in Table 4. As per the ASTM E23 standard, 27 or 40 J of energy absorbed is needed for the weldment to qualify the Charpy impact test (Ref. 20). It is clear from Table 4 that the impact toughness values of GMAW, SP-GMAW, and DP-GMAW are significantly higher than the minimum toughness required for the weld joint. It is noticed from Table 4 that the weldment made using the DP-GMAW technique has given comparatively higher impact toughness as compared to weldments made using the other two techniques, namely SP-GMAW and GMAW. The reduction in the grain size could be the primary reason for the higher impact toughness

value shown by the weldments made by DP-GMAW technique. Besides, the absence of carbide precipitates inveterates the improved toughness. The tensile and microhardness test confirmed a similar trend observed with impact toughness results. But the impact toughness absorbed by SP-GMAW is low and followed by GMAW. The existence of carbide precipitates and coarser crystallites size reduces the volume of grain boundaries, and this results in easy dislocation at the weld zone (Ref. 40).

4.8 EBSD Analysis

In this section, characteristics of microstructure and texture of the samples selected for EBSD analysis are discussed with the aid of IPF, Euler, GOS, and RF maps. The inverse pole figure (IPF) maps observed from the ND-RD section of the SP-GMAW, DP-GMAW, and base metal are illustrated in Fig. 18. The base metal revealed the equiaxed grains with twins within the majority of grains (Fig. 18(a)). Grain boundaries of majority of the grains are high angle in nature, and also it is

noticed that fine grains are formed along the grain boundaries (Fig. 18(b)). Based on the colour code of IPF given as insert in Fig. 18, the grains covered in the EBSD scan are random in orientation. Further, the IPF maps of the SP-GMAW and DP-GMAW display the dendritic structure. However, the SP-GMAW displays the broad and straight dendrites, whereas the scan from DP-GMAW weldment shown the formation of elongated as well as equiaxed dendrites of random orientations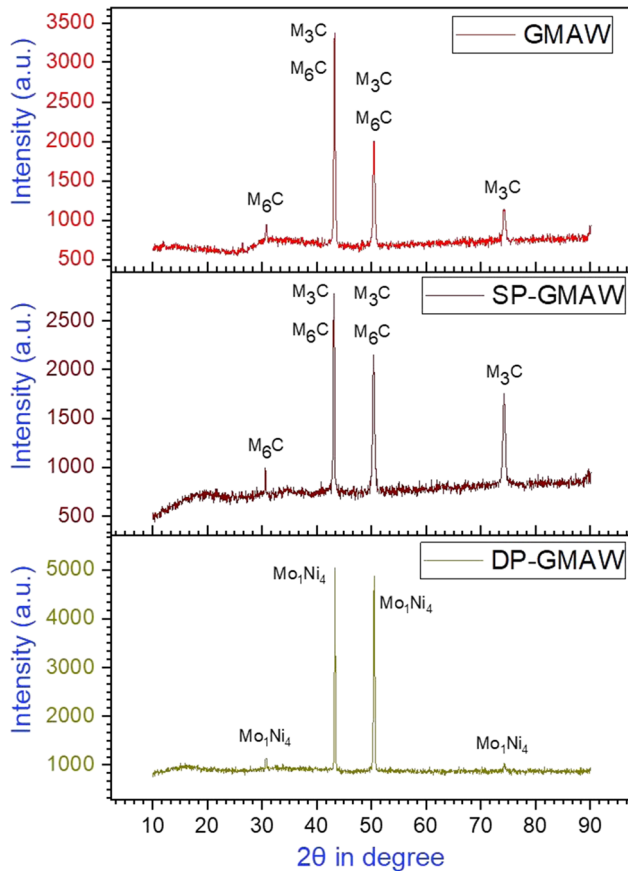 (Fig. 18(e) and (f). GOS and recrystallisation map for base metal and weldments from SP-GMAW as well as DP-GMAW are given in Fig. 19. GOS map in the measure of change in the degree of orientation between each pixel in the individual grain and its average orientation. This measurement can be linked to change in the lattice rotation due to strain imposed. Rainbow colour scale is given as an insert. Grains with a high level of strain, determined by the internal degree of lattice rotation, are coloured at the yellow-red portion of the rainbow colour scale given below the GOS maps (Ref. 41). Recrystallisation fraction maps presented in Fig. 19 gives information of the amount of recrystallised grains (blue), grains having sub-structure (yellow), and grains having a high level of dislocations (red) in the scanned area. Corresponding histograms illustrating the changes in its fraction are given as inserts in Fig. 19.

The inverse pole figure (Fig. 20) illustrates the orientation of grains that displays the profuse quantity of grain growth in $< 100 >$, $< 110 >$, and $< 111 >$ directions in the Hastelloy X (base metal) (Ref. 39, 42). This displays the strong alignment mixture of texture in $< 100 >$, $< 110 >$, and $< 111 >$. But, in weldments, the direction of grain growth and grain structure are primarily varied with the mode of welding technique like SP-GMAW and DP-GMAW, as displayed in Fig. 20. The IPF clearly shows that weldments of SP-GMAW have only one common $< 100 >$ direction for the entire solidification stages. It reveals that the solidification process predominantly starts at fusion boundary in $< 100 >$ direction and remains in the same direction $< 100 >$ for the entire process. However, the distinct outcomes are observed in DP-GMAW techniques. IPF of the DP-GMAW depicts the major intensity shift from $< 100 >$ to $< 111 >$ direction. Further, IPF displays the shift in secondary intensity grain growth from $< 100 >$ to $< 111 >$ direction. This is mostly due to the rotation of grains towards its preferable grain growth direction (Ref. 3, 43).

The orientation distribution function (ODF) derived from EBSD scans made on the base metal, SP-GMAW, and DP-GMAW at three different $\phi_2 = 45°$ sections of Euler space is shown in Fig. 20 (a-c), respectively. $\phi_2 = 45°$ section showing ideal texture components and fibres are given in Fig. 20(d). Characteristic of texture shown by $\phi_2 = 45°$ section of ODF for the base metals is similar to the one observed in the case of hot-rolled FCC material. The $\phi_2 = 45°$ section of base metal depicts the strong intensities around the locations of ideal brass ($\{110\} < \bar{1}\bar{1}2 >$), γ-fibre ($\{111\} < 1\bar{2}1 >$ and $\{111\} < \bar{1}\bar{1}2 >$), and copper ($\{112\} < \bar{1}\bar{1}\bar{1} >$), whereas the $\phi_2 = 45°$ section of

Fig. 15 XRD peaks of Hastelloy X welded by GMAW, SP-GMAW, and DP-GMAW-ERNiCrMo-2

Table 3 Tensile properties of base metal, and weldments by three welding techniques

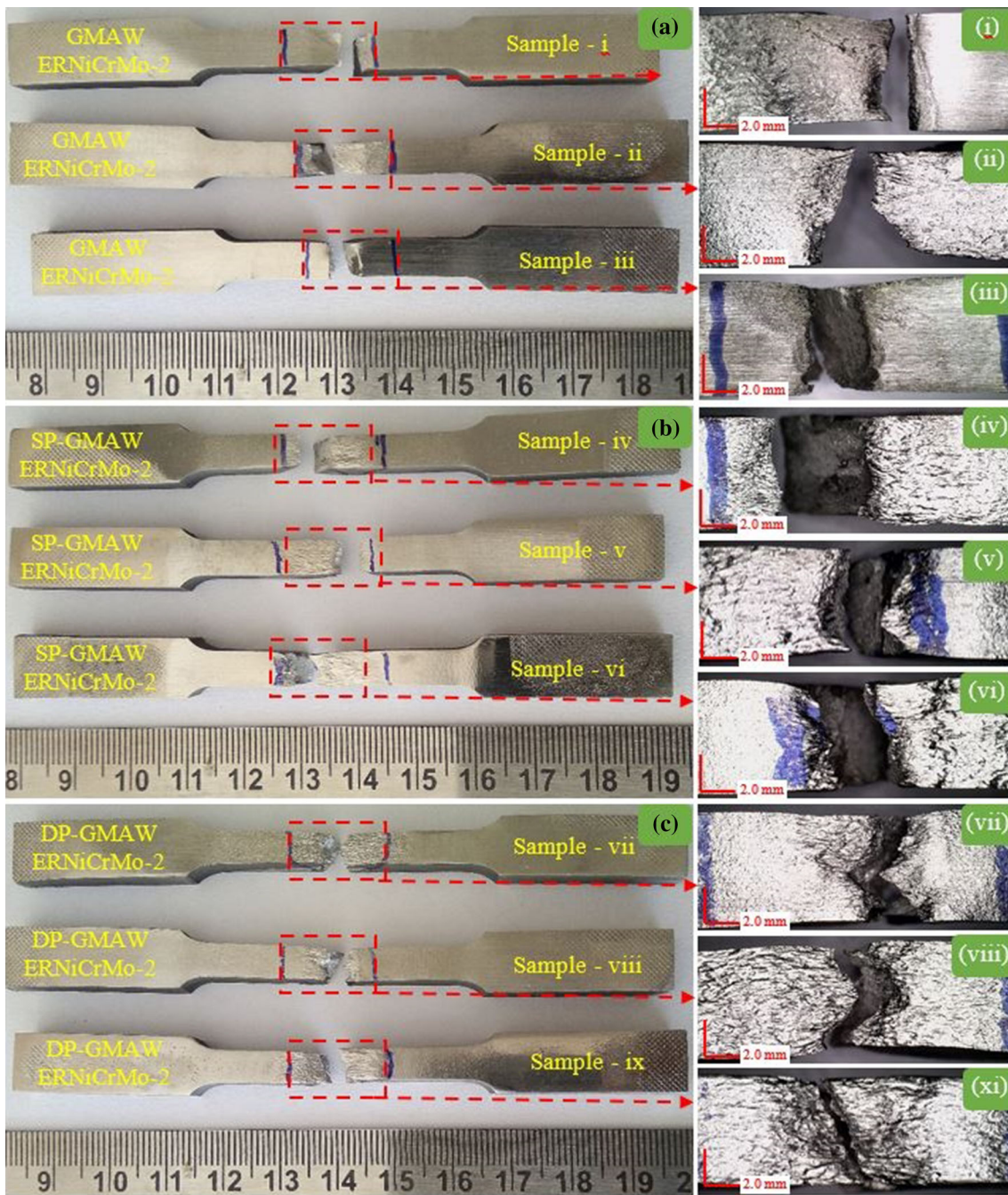| Material	UTS, MPa	Mean UTS, MPa	0.2% PS, MPa	Mean 0.2% PS, MPa	Elongation, %	Mean elongation, %
Base metal	793	790 ± 3.1	363	322 ± 4.1	46	46 ± 0.6
	789		358		46	
	787		355		45	
GMAW weldment	619	624 ± 5.0	322	325 ± 3.5	15	16 ± 1
	629		329		17	
	625		325		16	
SP-GMAW weldment	694	688 ± 6.0	341	338 ± 3.1	27	25 ± 1.5
	688		339		24	
	682		335		25	
DP-GMAW weldment	768	761 ± 6.5	357	353 ± 4.7	36	37 ± 1
	755		348		37	
	761		355		38	

Fig. 16 Tensile fractured images of Hastelloy X welded by (a) GMAW-ERNiCrMo-2, (b) SP-GMAW-ERNiCrMo-2, and (c) DP-GMAW-ERNiCrMo-2

SP-GMAW condition depicts the intensity of copper ({112} $<\bar{1}\bar{1}\bar{1}>$) orientations. Formation of γ-fibre is triggered by the recrystallisation process occurring in the weldments. Evidence of brass texture in DP-GMAW displays slightly different texture compared to SP-GMAW weldment due to the presence of long dendrites. Due to the formation of new equiaxed grains of different orientations by dynamic recrystallisation in the case of SP-GMAW weldment, γ-fibre started developing, which is confirmed in Fig. 20 (c). This randomness in the grain orientations of the weldments is mainly attributed by the

steeper thermal gradient, speedy cooling rate obtained during solidification (Ref. 3).

During solidification, the mode of transfer and type of welding technique (GMAW, SP-GMAW, and DP-GMAW) which have a strong influence on changes in the direction of grain growth. Further, the weld pool shaper is mostly influenced by the mode of metal transfer, which primarily alters the grain growth. In DP-GMAW, the continuous changes in the current pulsing lead to periodic changes in driving forces and maximum turbulence in the weld pool, which can decrease the interface temperature of solidification. The better mechanical

properties observed in DP-GMAW compared to GMAW and SP-GMAW is due to the high amplitude thermal oscillations that occurred at the weld pool region. The thermal fluctuations in double pulsing conditions lead to periodic changes in the weld pool shape and size, which results in the development of new grains in WC. These new grains are regularly oriented along with the directions of a steeper thermal gradient, which results in the shifting of preferred grain growth direction (Ref. 43). Hence, the results conclude that solidifications during DP-GMAW initially proceed in the base metal grain direction $< 100 >$ next to the fusion boundary. Then, it is shifted or deviated from $< 100 >$ direction due to the higher turbulence in fluid flow.

5. Conclusions

The welding of Hastelloy X has been performed using GMAW, SP-GMAW, and DP-GMAW techniques with ER-NiCrMo-2. The weldment characterisation has also been evaluated besides with its mechanical properties. From this study, the following conclusions have arrived.

1. The weldments made with GMAW, SP-GMAW, and DP-GMAW found defect-free. Besides, the top width to depth of penetration ratio for DP-GMAW is the lowest (1.455) when compared to weldments by SP-GMAW (1.544) and GMAW (1.634) techniques.
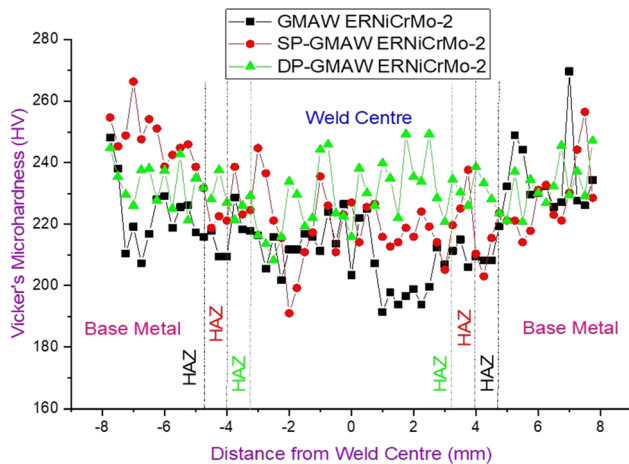

Fig. 17 Microhardness graphs of Hastelloy X welded by GMAW-ERNiCrMo-2, SP-GMAW-ERNiCrMo-2, and DP-GMAW-ERNiCrMo-2

2. A low rate of the constitutional cooling rate experienced by GMAW weldments leads to the formation of cellular dendrites. Whereas, the better constitutional cooling rate observed in DP-GMAW and SP-GMAW promotes the fine equiaxed dendrites. It is pointed out by heterogeneous nucleation, dendrite refinement or fragmentation, and dendrite detachment mechanism.

3. Mo-rich segregations are identified in the interdendritic region of GMAW owing to high solidification time that provides sufficient time for Mo-rich elements to segregate at interdendritic. It is reduced for SP-GMAW, whereas it is completely precluded for DP-GMAW due to the existence of refined grain, which has a higher grain boundary area because of low free energy.

4. The development of M_3C (Fe_2MoC) and M_6C (Fe_2Mo_4C) carbide precipitates is observed for GMAW and SP-GMAW. It is observed in the script shapes, coarse cubic, and acicular form that fail easily. But, DP-GMAW displays better mechanical strength due to the absence of Mo-rich carbides and the development of Mo_1Ni_4 intermetallic precipitates. Besides, refined crystallite grains are observed in DP-GMAW.

5. DP-GMAW provides better joint efficiency, which led to better UTS as well as ductility, compared to SP-GMAW and GMAW. This is due to the formation of fine equiaxed dendrites with smaller crystallite grains along with Mo_1Ni_4 intermetallic precipitates observed in DP-GMAW.

6. DP-GMAW shows 7.31% and 3.52% higher mean microhardness with respect to GMAW and SP-GMAW, respectively. Further, the maximum impact toughness is observed in DP-GMAW (76 ± 3.1 J) with respect to SP-GMAW (60 ± 2.1 J) and GMAW (51 ± 1.2 J) techniques.

7. Inverse pole figure maps from EBSD scans done on DP-GMAW shows the major intensity shift from $< 100 >$ to $< 111 >$ direction. ODF of DP-GMAW depicts significant random orientations of grains due to a decrease in solidifying interface temperature.

From this study, it is clear that DP-GMAW provided the better mechanical and metallurgical results compared to GMAW and SP-GMAW. Hence, DP-GMAW is recommended for welding of Hastelloy X used in aerospace applications (Boeing aircraft combustion chamber parts of JT9D turbojet engine).

Table 4 Impact toughness of base metal, and weldments by three welding techniques

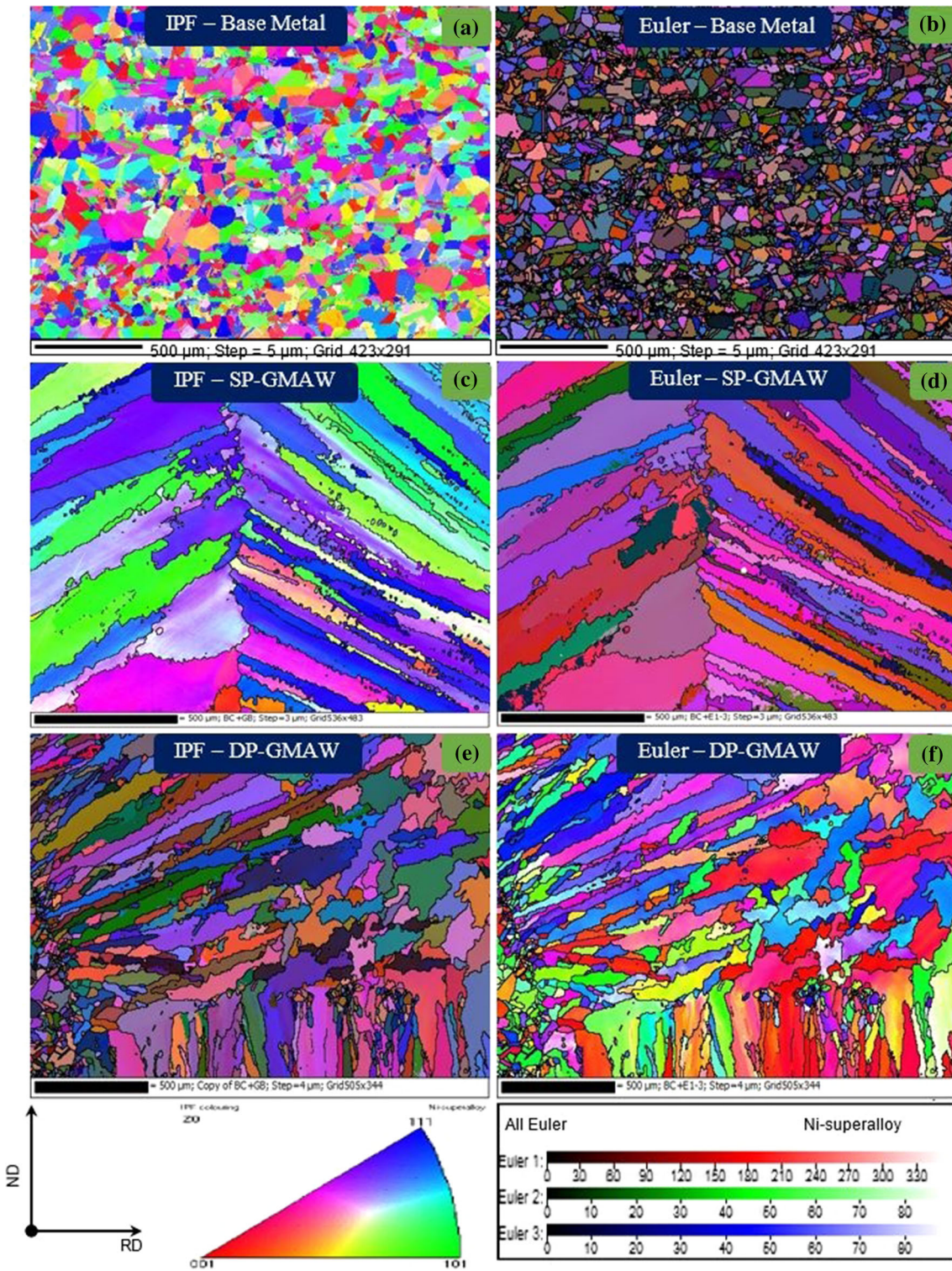| Material condition	Impact energy absorbed, J			
	Sample 1	Sample 2	Sample 3	Mean impact energy absorbed, J
Base metal	88	86	80	85 ± 4.2
GMAW weldment	52	50	52	51 ± 1.2
SP-GMAW weldment	62	59	58	60 ± 2.1
DP-GMAW weldment	78	72	76	76 ± 3.1

Fig. 18 IPF and Euler maps of base metals and weldments; (a, b) Hastelloy X, (c, d) SP-GMAW-ERNiCrMo-2, and (e, f) DP-GMAW-ERNiCrMo-2
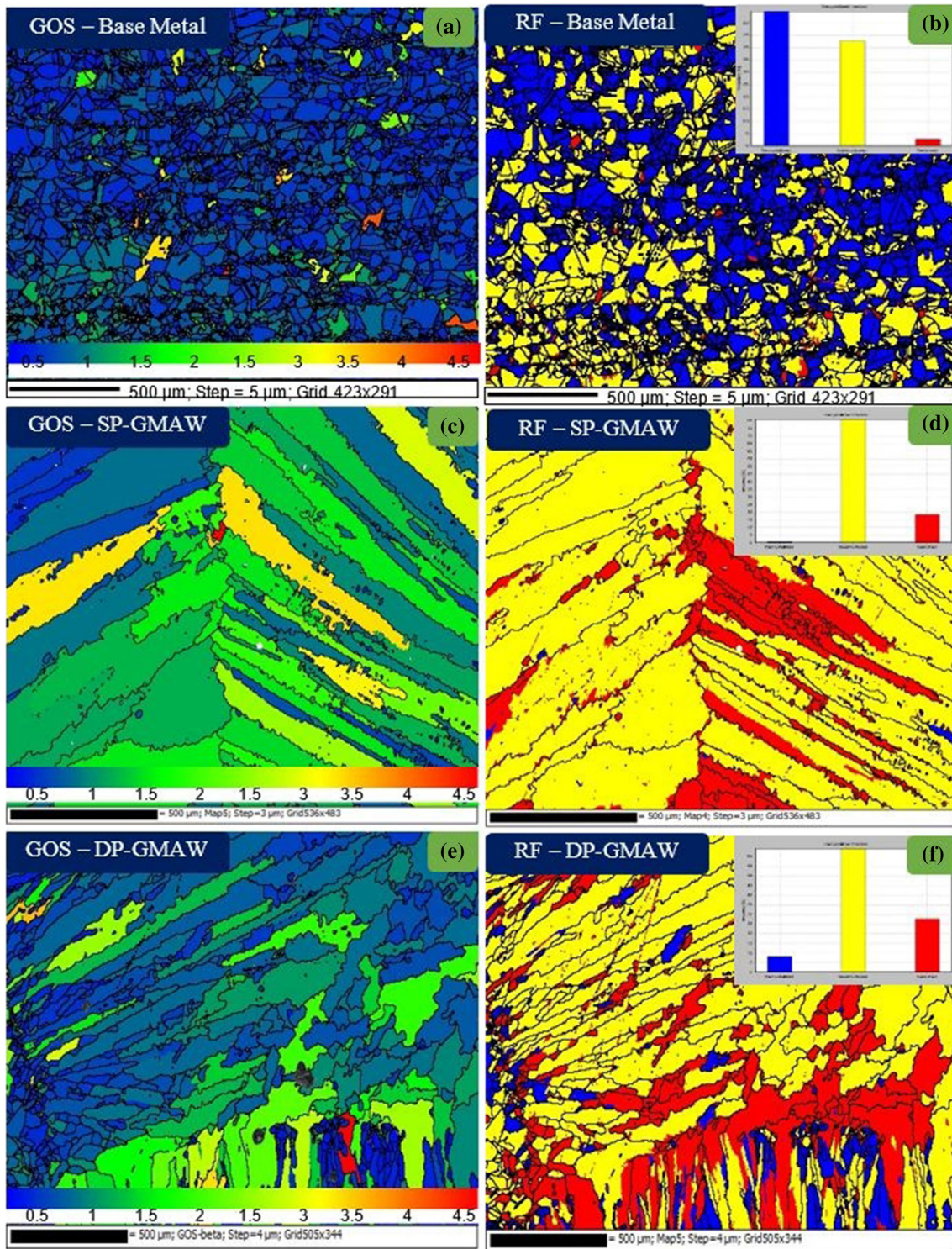
Fig. 19 Grain orientation spread (GOS) and recrystallisation fraction (RF) maps of base metals and weldments; (a, b) Hastelloy X, (c, d) SP-GMAW-ERNiCrMo-2, and (e, f) DP-GMAW-ERNiCrMo-2
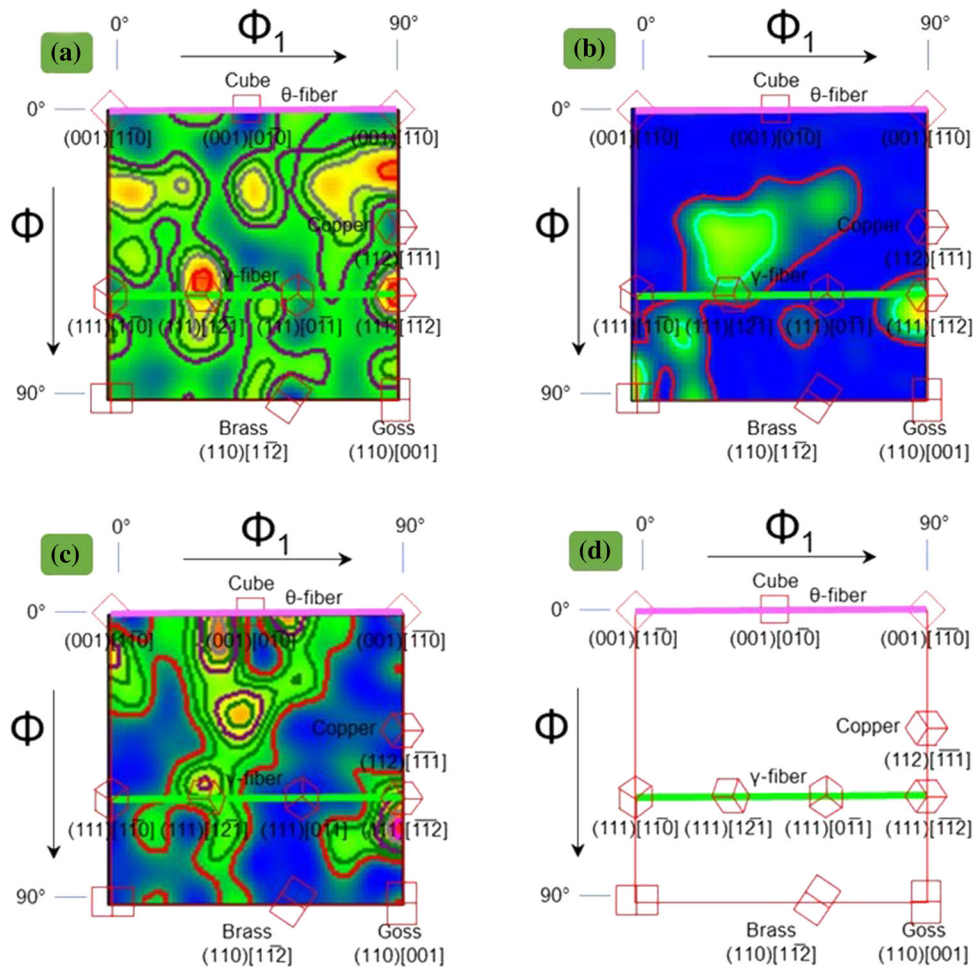
Fig. 20 $\phi_2 = 45°$ sections of orientation distribution function (ODF) grains in base metals and weldments; (a) Hastelloy X, (b) SP-GMAW-ERNiCrMo-2, (c) DP-GMAW-ERNiCrMo-2, and (d) $\phi_2 = 45°$ section showing ideal texture components and fibres

References

1. Inconel alloy HX (UNS N06002), Technical Data Sheet, Special Metal Corporation (2005). http://www.specialmetals.com/assets/smc/documents/alloys/inconel/inconel-alloy-hx.pdf. Accessed 10 Mar 2020
2. G.V.P. Reddy, P. Harini, R. Sandhya, K.B.S. Rao, and R.K. Paretkar, On Dual-Slope Linear Cyclic Hardening of Hastelloy X, *Mater. Sci. Eng. A*, 2010, **527**(16–17), p 3848–3851. https://doi.org/10.1016/j.msea.2010.02.062
3. Q. Han, R. Mertens, M.L. Montero-Sistiaga, S. Yang, R. Setchi, K. Vanmeensel, B. Van Hooreweder, S.L. Evans, and H. Fan, Laser Powder Bed Fusion of Hastelloy X: Effects of Hot Isostatic Pressing and the Hot Cracking Mechanism, *Mater. Sci. Eng. A*, 2018, **732**, p 228–239. https://doi.org/10.1016/j.msea.2018.07.008
4. M. Sathishkumar and M. Manikandan, Hot Corrosion Behaviour of Continuous and Pulsed Current Gas Tungsten Arc Welded Hastelloy X in Different Molten Salts Environment, *Mater. Res. Express*, 2019, **6**(12), p 126553. https://doi.org/10.1088/2053-1591/ab562a
5. W.G. Kim, S.N. Yin, W.S. Ryu, J.H. Chang, and S.J. Kim, Tension and Creep Design Stresses of the "Hastelloy-X" Alloy for High-Temperature Gas Cooled Reactors, *Mater. Sci. Eng. A*, 2008, **483–484**, p 495–497. https://doi.org/10.1016/j.msea.2006.12.184
6. C. Chen, C. Fan, S. Lin, X. Cai, L. Zhou, S. Ye, and C. Yang, E Ff Ect of Ultrasonic Pattern on Weld Appearance and Droplet Transfer in Ultrasonic Assisted MIG Welding Process, *J. Manuf. Process.*, 2018, **35**(92), p 368–372. https://doi.org/10.1016/j.jmapro.2018.08.019
7. D. Li, D. Yang, G. Zhang, X. Chen, and X. Luo, Microstructure and Mechanical Properties of Welding Metal with High Cr-Ni Austenite Wire through Ar-He-N2 Gas Metal Arc Welding, *J. Manuf. Process.*, 2018, **35**(92), p 190–196. https://doi.org/10.1016/j.jmapro.2018.07.026
8. X. Ni, D. Kong, L. Zhang, C. Dong, J. Song, and W. Wu, Effect of Process Parameters on the Mechanical Properties of Hastelloy X Alloy Fabricated by Selective Laser Melting, *J. Mater. Eng. Perform.*, 2019, **28**(9), p 5533–5540. https://doi.org/10.1007/s11665-019-04275-w
9. N. Aminipour and R. Derakhshandeh-Haghighi, The Effect of Weld Metal Composition on Microstructural and Mechanical Properties of Dissimilar Welds Between Monel 400 and Inconel 600, *J. Mater. Eng. Perform.*, 2019, **28**(10), p 6111–6124. https://doi.org/10.1007/s11665-019-04328-0
10. M. Sathishkumar and M. Manikandan, Development of Pulsed Current Arc Welding to Preclude Carbide Precipitates in Hastelloy X Weldment Using ERNiCr-3, *J. Mater. Eng. Perform.*, 2020, **29**(8), p 5395–5408. https://doi.org/10.1007/s11665-020-05010-6
11. O.A. Ojo and M.C. Chaturvedi, Liquation Microfissuring in the Weld Heat-Affected Zone of an Overaged Precipitation-Hardened Nickel-Base Superalloy, *Metall, Mater. Trans. A Phys. Metall. Mater. Sci.*, 2007, **26**, p 356–369. https://doi.org/10.1007/s11661-006-9025-1
12. E.R. Baek, S.S. Park, R.S. Sihotang, and S.K. Choi, Heat Treatment of the Degraded Hastelloy-X for High Cycle Fatigue Properties, in *Proceedings of the 9th International Conference on Fracture and the Strength of Solids*, (jeju), 2013, p 91

13. R. Sihotang, P. Sung-Sang, and B. Eung-Ryul, Effects of Heat Input on Microstructure of Tungsten Inert Gas Welding Used Hastelloy X, *Mater. Res. Innov.*, 2014, **18**, p S2-1074–S2-1080. https://doi.org/10.1179/1432891714z.000000000559

14. M.R. Abedi, H. Sabet, and H. Razavi, The Effect of Repair Welding Number on Microstructure of Hastelloy X Fabricated via TIG Process, *Int. J. Mater. Sci. Appl.*, 2016, **5**(2), p 43–48. https://doi.org/10.11648/j.ijmsa.20160502.12

15. J.C. Zhao, M. Larsen, and V. Ravikumar, Phase Precipitation and Time-Temperature-Transformation Diagram of Hastelloy X, *Mater. Sci. Eng. A*, 2000, **293**(1), p 112–119. https://doi.org/10.1016/S0921-5093(00)01049-2

16. S. Shimizu and Y. Mutoh, Weldability and Weld Performance of a Special Grade Hastelloy-X Modified for High-Temperature Gas-Cooled Reactors, *Nucl. Technol.*, 1984, **66**(1), p 44–53. https://doi.org/10.13182/NT84-A33453

17. D. Tomus, P.A. Rometsch, M. Heilmaier, and X. Wu, Effect of Minor Alloying Elements on Crack-Formation Characteristics of Hastelloy-X Manufactured by Selective Laser Melting, *Addit. Manuf.*, 2017, **16**, p 65–72. https://doi.org/10.1016/j.addma.2017.05.006

18. K. Pal and S.K. Pal, Effect of Pulse Parameters on Weld Quality in Pulsed Gas Metal Arc Welding: A Review, *J. Mater. Eng. Perform.*, 2011, **20**(6), p 918–931. https://doi.org/10.1007/s11665-010-9717-y

19. M. Sen, M. Mukherjee, S. Kumar, and T. Kumar, Effect of Double-Pulsed Gas Metal Arc Welding (DP-GMAW) Process Variables on Microstructural Constituents and Hardness of Low Carbon Steel Weld Deposits, *J. Manuf. Process.*, 2018, **31**, p 424–439. https://doi.org/10.1016/j.jmapro.2017.12.003

20. M. Sathishkumar and M. Manikandan, Influence of Pulsed Current Arc Welding to Preclude the Topological Phases in the Aerospace Grade Alloy X, *Proc. Inst. Mech. Eng. Part L J. Mater. Des. Appl.*, 2020, **234**(4), p 637–653. https://doi.org/10.1177/1464420720907993

21. M. Sathishkumar and M. Manikandan, Preclusion of Carbide Precipitates in the Hastelloy X Weldment Using the Current Pulsing Technique, *J. Manuf. Process.*, 2019, **45**, p 9–21. https://doi.org/10.1016/j.jmapro.2019.06.027

22. L.L. Wang, H.L. Wei, J.X. Xue, and T. Debroy, Special Features of Double Pulsed Gas Metal Arc Welding, *J. Mater. Process. Tech.*, 2018, **251**, p 369–375. https://doi.org/10.1016/j.jmatprotec.2017.08.039

23. L.L. Wang, H.L. Wei, J.X. Xue, and T. Debroy, A Pathway to Microstructural Re Finement through Double Pulsed Gas Metal Arc Welding, *Scr. Mater.*, 2017, **134**, p 61–65. https://doi.org/10.1016/j.scriptamat.2017.02.034

24. A. Liu, X. Tang, and F. Lu, Study on Welding Process and Prosperities of AA5754 Al-Alloy Welded by Double Pulsed Gas Metal Arc Welding, *Mater. Des.*, 2013, **50**, p 149–155. https://doi.org/10.1016/j.matdes.2013.02.087

25. A. Mathivanan, A. Senthilkumar, and K. Devakumaran, Pulsed Current and Dual Pulse Gas Metal Arc Welding of Grade AISI, : 310S Austenitic Stainless Steel, *Def. Technol.*, 2015, **11**(3), p 269–274. https://doi.org/10.1016/j.dt.2015.05.006

26. P.K. Palani and N. Murugan, Selection of Parameters of Pulsed Current Gas Metal Arc Welding, *Joutnal Mater. Process. Technol.*, 2006, **172**, p 1–10. https://doi.org/10.1016/j.jmatprotec.2005.07.013

27. K. Wu, N. Ding, T. Yin, M. Zeng, and Z. Liang, Effects of Single and Double Pulses on Microstructure and Mechanical Properties of Weld Joints during High-Power Double-Wire GMAW, *J. Manuf. Process.*, 2018, **35**, p 728–734. https://doi.org/10.1016/j.jmapro.2018.08.025

28. S. Krishnan, D.V. Kulkarni, and A. De, Probing Pulsed Current Gas Metal Arc Welding for Modified 9Cr-1Mo Steel, *J. Mater. Eng. Perform.*, 2015, **24**(4), p 1462–1470. https://doi.org/10.1007/s11665-015-1430-4

29. M. Sathishkumar, C.D. Naiju, and M. Manikandan, Investigation of Metallurgical and Mechanical Properties of Hastelloy X by Key-Hole Plasma Arc Welding Process, *SAE Tech. Pap.*, 2019, **2019-28–0152**, p 1–5. https://doi.org/10.4271/2019-28-0152

30. V.K. Goyal, P.K. Ghosh, and J.S. Saini, Analytical Studies on Thermal Behaviour and Geometry of Weld Pool in Pulsed Current Gas Metal Arc Welding, *J. Mater. Process. Technol.*, 2009, **09**, p 318–1336. https://doi.org/10.1016/j.jmatprotec.2008.03.035

31. J. Yi, S. Cao, L. Li, P. Guo, and K. Liu, Effect of Welding Current on Morphology and Microstructure of Al Alloy T-Joint in Double-Pulsed MIG Welding, *Trans. Nonferrous Met. Soc. China*, 2015, **25**(10), p 3204–3211. https://doi.org/10.1016/s1003-6326(15)63953-x

32. J.N. Dupont, Fundamentals of Weld Solidification, *ASM Handbook-Weld. Fundam. Process.*, 2011, **6A**, p 96–114. https://doi.org/10.31399/asm.hb.v06a.a0005609

33. Y. Wang, B. Qi, and B. Cong, Arc Characteristics in Double-Pulsed VP-GTAW for Aluminum Alloy, *J. Mater. Process. Tech.*, 2017, **249**(January), p 89–95. https://doi.org/10.1016/j.jmatprotec.2017.05.027

34. S. Zhou, D. Chai, J. Yu, G. Ma, and D. Wu, Microstructure Characteristic and Mechanical Property of Pulsed Laser Lap-Welded Nickel-Based Superalloy and Stainless Steel, *J. Manuf. Process.*, 2017, **25**, p 220–226. https://doi.org/10.1016/j.jmapro.2016.11.010

35. K. Sindo, *Welding Metallurgy*, 2nd ed., New York, Wiley, 2003, https://doi.org/10.1016/j.theochem.2007.07.017

36. M. Pakniat, F.M. Ghaini, and M.J. Torkamany, Hot Cracking in Laser Welding of Hastelloy X with Pulsed Nd:YAG and Continuous Fiber Lasers, *Mater. Des.*, 2016, **106**, p 177–183. https://doi.org/10.1016/j.matdes.2016.05.124

37. Z. Xu, L. Jiang, J. Dong, Z. Li, and X. Zhou, The Effect of Silicon on Precipitation and Decomposition Behaviors of M6C Carbide in a Ni-Mo-Cr Superalloy, *J. Alloys Compd.*, 2015, **620**, p 197–203. https://doi.org/10.1016/j.jallcom.2014.09.112

38. R. Sihotang, S. Choi, S. Park, and E. Baek, Fatigue Life of the Repair TIG Welded Hastelloy X Superalloy, *J. Weld. Join.*, 2015, **33**(5), p 26–30. https://doi.org/10.5781/JWJ.2015.33.5.26

39. D. Tomus, Y. Tian, P.A. Rometsch, M. Heilmaier, and X. Wu, Influence of Post Heat Treatments on Anisotropy of Mechanical Behaviour and Microstructure of Hastelloy-X Parts Produced by Selective Laser Melting, *Mater. Sci. Eng. A*, 2016, **667**(4), p 42–53. https://doi.org/10.1016/j.msea.2016.04.086

40. B. Arulmurugan and M. Manikandan, Development of Welding Technology for Improving the Metallurgical and Mechanical Properties of 21st Century Nickel Based Superalloy 686, *Mater. Sci. Eng. A*, 2017, **691**, p 126–140. https://doi.org/10.1016/j.msea.2017.03.042

41. W.Z. Abuzaid, M.D. Sangid, J.D. Carroll, H. Sehitoglu, and J. Lambros, Slip Transfer and Plastic Strain Accumulation across Grain Boundaries in Hastelloy X, *J. Mech. Phys. Solids*, 2012, **60**(6), p 1201–1220. https://doi.org/10.1016/j.jmps.2012.02.001

42. J. Graneix, J.-D. Beguin, F. Pardheillan, J. Alexis, and T. Masri, Weldability of the Superalloys Haynes 188 and Hastelloy X by Nd:YAG, *Eurosuperalloys 2014-Nd Eur. Symp. Superalloys Their Appl.*, 2014, **14**, https://doi.org/10.1051/matecconf/20141413006

43. M. Mukherjee, S. Saha, T.K. Pal, and P. Kanjilal, Influence of Modes of Metal Transfer on Grain Structure and Direction of Grain Growth in Low Nickel Austenitic Stainless Steel Weld Metals, *Mater. Charact.*, 2015, **102**, p 9–18. https://doi.org/10.1016/j.matchar.2015.02.006

Publisher's Note Springer Nature remains neutral with regard to jurisdictional claims in published maps and institutional affiliations.